

A new WENO-based momentum advection scheme for simulations of ocean mesoscale turbulence

Simone Silvestri¹, Gregory L. Wagner¹, Jean-Michel Campin¹,
 Navid C. Constantinou², Christopher N. Hill¹,
 Andre Souza¹, and Raffaele Ferrari¹

¹Massachusetts Institute of Technology, Cambridge, MA, USA

²Australian National University, Canberra, ACT, Australia

Key Points:

- We describe a new momentum advection scheme based on upwind-biased, weighted essentially non-oscillatory (WENO) reconstructions.
- The new scheme automatically adapts to horizontal resolution, does not generate grid-scale noise, and minimizes energy dissipation.
- The new scheme delivers a higher “effective” resolution compared to a second-order scheme stabilized by explicit dissipation.

Abstract

Current eddy-permitting and eddy-resolving ocean models require dissipation to prevent a spurious accumulation of enstrophy at the grid scale. We introduce a new numerical scheme for momentum advection in large-scale ocean models that involves upwinding through a weighted essentially non-oscillatory (WENO) reconstruction. The new scheme provides implicit dissipation and thereby avoids the need for an additional parameterization for explicit dissipation that may require calibration of unknown parameters. This approach uses the rotational, “vector invariant” formulation of the momentum advection operator that is widely employed by global general circulation models. A novel formulation of the WENO “smoothness indicators” is key for avoiding excessive numerical dissipation of kinetic energy and enstrophy at grid-resolved scales. We test the new advection scheme against a standard approach that combines explicit subgrid-scale dissipation with a dispersive discretization of the rotational advection operator in two scenarios: (*i*) two-dimensional turbulence and (*ii*) three-dimensional baroclinic equilibration. In both cases the solutions are stable, free from dispersive artifacts and achieve increased “effective” resolution compared to standard methods.

Plain Language Summary

High-resolution climate models that resolve the cyclones and anticyclones in the ocean, often called “eddies”, must prevent an artificial build-up of whirl-like movements, or “enstrophy”, at the model’s grid-scale. But even though methods that prevent artificial accumulation of enstrophy are included only to ensure numerical stability, they unfortunately also negatively impact the quality of the model predictions even at scales larger than the grid-scale. Here, we devise a novel numerical method to overcome this deficiency. Our method has the best of both worlds: it removes just enough enstrophy so that the flow is as close to reality as possible and it achieves this without accumulating enstrophy at grid-scale.

Corresponding author: Simone Silvestri, silvestri.simone0@gmail.com

1 Introduction

Mesoscale ocean turbulence, characterized by eddies ranging from 10 to 100 kilometers in size, plays a crucial role in mixing heat, salt, momentum, and biogeochemical tracers throughout the ocean. This mixing in turns exerts a leading-order control on the large-scale ocean circulation and its impact on climate (Vallis, 2017). Until recently, climate models used ocean grids coarser than 100 km and resorted to parameterize this turbulence. The existing parameterizations (Gent & Mcwilliams, 1990) remain quite uncertain and contribute significant uncertainties to climate projections. In the last few years it has become possible to run global ocean simulations with fine grids in the 10–25 km range that partially resolve the mesoscale turbulence. This resolution is referred to as “eddy-permitting” in contrast to the “eddy-resolving” resolution that requires even finer grids, beyond presently available computational resources for climate projections (Ding et al., 2022; Silvestri et al., 2023). The eddy-permitting regime shares conceptual similarities with the well-established Large Eddy Simulation (LES) technique used in computational fluid dynamics for three-dimensional turbulence. In both cases the grid resolution resolves only the largest turbulent eddies. The goal of this paper is to exploit this similarity and develop a more accurate numerical scheme for mesoscale turbulence.

We start by illustrating that the numerical schemes typically used to represent subgrid-scale physics in “eddy-permitting” mesoscale simulations (Smagorinsky, 1963; Leith, 1996) generate substantial noise at the grid scale which is then controlled with diffusive operators. This reduces the effective resolution of the simulation, because the smallest scales are compromised by numerics, and may even affect the accuracy of the large-scale solutions since the mesoscale regime is characterized by a vigorous inverse energy cascade. Here, we introduce a LES-inspired numerical scheme that minimizes both the energy dissipation and the noise at the grid scale, thereby increasing the effective resolution of the model and improving numerical stability. Even more appealing is that the scheme holds the promise to reduce the computational cost of “eddy-resolving” simulations which could be achieved with coarser grids than with presently used schemes.

By design, LES allows large-scale turbulence, or eddies, to spontaneously emerge due to nonlinear interactions in the resolved flow. As such, LES requires a closure model for subgrid-scale (SGS) physics to coexist with larger-scale motions whose nonlinear interactions are resolved. An SGS closure should adhere to five fundamental principles:

- (1) **Convergence:** The ultimate goal of any SGS closure is to reproduce the exact solution to the governing equations. Therefore, an SGS closure should smoothly turn off as the resolution becomes sufficiently fine to resolve the smallest scales of turbulence.
- (2) **Flow-awareness:** Turbulence is characterized by intricate interactions between various scales, where regions of large gradients are usually associated with increased subgrid-scale motion. Hence, to be accurate, SGS closures must adapt to the local flow properties.
- (3) **Variance removal at the grid-scale:** Numerical models are characterized by noise generated by small-scale fluctuations and numerical disturbances that can introduce errors or instability into the simulation. A good SGS closure must be able to dissipate this noise effectively without affecting the accuracy of the solution at larger scales.
- (4) **Adjustment to varying resolution:** An SGS closure should adapt to the resolution of the problem, providing correct and consistent solutions, irrespective of the grid size. This ensures the closure remains accurate across diverse scales.
- (5) **Performance:** Ultimately, the adoption of an SGS closure depends on its stability and performance. Closures that are prone to generating instabilities, require extensive tuning or considerably slow down the simulation may discourage their application in comprehensive ocean models.

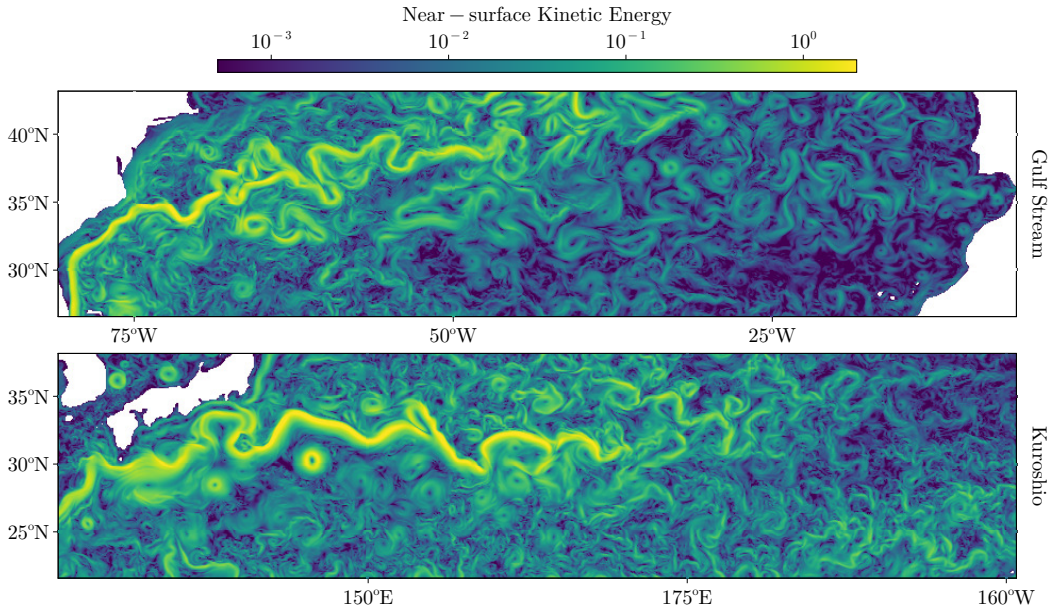


Figure 1. Near-surface kinetic energy in the Gulf stream (top panel) and the Kuroshio current (bottom panel) on March 1st from a global ocean simulation at 1/12-th of a degree horizontal resolution and 100 vertical levels that uses the novel advection scheme we introduce here as a momentum closure.

SGS closures fall into two categories: explicit and implicit. Typical explicit LES attempt to predict the rate of variance destruction through a diffusive approximation. Explicit closures for mesoscale turbulence have been inspired by eddy closures developed for highly resolved LES for isotropic, homogeneous, three- and two-dimensional turbulence (Smagorinsky, 1963; Fox-Kemper & Menemenlis, 2004; Bachman et al., 2017). Conversely, an implicit SGS closure, or *Implicit Large Eddy Simulation* (ILES), relies on the truncation errors introduced by the numerical discretization to provide the necessary subgrid-scale diffusion, i.e., $\nabla \cdot \tau_{\text{SGS}} \approx \mathcal{N}$, where $\nabla \cdot \tau_{\text{SGS}}$ is the divergence of the subgrid-scale fluxes and \mathcal{N} is the truncation error introduced by the discretization scheme. This methodology is referred to as “implicit” since the subgrid-scale closure is incorporated implicitly through the numerical discretization. Employing the ILES approach has the benefit of circumventing one of the main downsides of an explicit closure: the necessity of calibrating unknown free parameters to accurately simulate SGS fluxes. More importantly, ILES suppresses spurious numerical modes caused by dispersion errors typical of centered reconstruction schemes. On the contrary, explicit closures formulated in terms of an adaptive “eddy” viscosity often require additional tweaking to damp the spurious computational modes. This reduces the accuracy in the representation of the SGS fluxes, resulting in a lower “effective” resolution (Pressel et al., 2017).

ILES is designed such that the numerical truncation error \mathcal{N} , inherent in the discretization scheme, approximates the SGS fluxes at small scales. This typically involves diffusing or “mixing” the momentum associated with resolved eddies which means adopting a scheme that is characterized by a diffusive numerical truncation at the leading order. Examples include flux-limited advection (Van Leer, 1977; Zalesak, 1979), piecewise-parabolic methods (Woodward & Colella, 1984; Sytine et al., 2000), semi-Lagrangian advection (Bates & McDonald, 1982), and essentially non-oscillatory schemes (Osher & Shu, 1991). A challenge in applying ILES to the mesoscale turbulence problem is that the SGS fluxes are not dissipative, but rather inject energy onto the resolved scales (Juricke et al., 2019). Explicit diffusive closures, commonly used in ocean modeling, are also deficient when it comes to dealing with this backscatter of energy onto the resolved scales. Here we take the position that ILES prevent the spurious accumulation of numerical noise at the smallest scales and thus converge

to the exact solution at “eddy-resolving” resolutions. At “eddy-permitting” resolutions a parameterization for energy backscatter may still be necessary, but without the additional complication of having to confront grid-scale noise.

The ILES approach has seen wide application in combination with the conservative (or “flux-form”) formulation of the advection operator (Karaca et al., 2012; Maulik & San, 2018; Zeng et al., 2021), including in atmospheric models (Smolarkiewicz & Margolin, 1998; Souza et al., 2023; Norman et al., 2023) and regional ocean models (Shchepetkin & McWilliams, 1998a; Holland et al., 1998; Mohammadi-Aragh et al., 2015). However, finite-volume general circulation models (GCMs) often favor the rotational formulation of the advection operator due to its ease of implementation with non-regular grids, such as the cubed sphere grid (Ronchi et al., 1996), the latitude-longitude capped grid (Fenty & Wang, 2020), or the tripolar grid (Madec & Imbard, 1996). Within the rotational framework, the application of upwinding-based ILES is far less common. Hahn and Iaccarino (2008) introduced upwinding in the rotational three-dimensional Navier–Stokes equations applied to the kinetic energy gradient, while Ringler (2011) described the upwinding of vorticity in the vorticity flux term as a possible monotone, diffusive discretization of the advection operator in the rotational form. The latter approach, which aligns more with the intrinsic dynamics of two-dimensional flows that are characterized by a forward enstrophy cascade, has been implemented by Roullet and Gaillard (2022) in the rotational form of the shallow-water equations using a weighted essentially non-oscillatory (WENO) reconstruction scheme.

Despite this recent progress, a mature formulation of a rotational-based ILES for the primitive equations¹ solved by GCMs, is still lacking. Here, we take inspiration from Roullet and Gaillard (2022) and develop a WENO reconstruction scheme tailored to the rotational formulation of the advection operator, applicable to both the two-dimensional Navier–Stokes and the primitive equations. We propose this scheme as an alternative to the commonly used approach for tackling mesoscale turbulence in eddy-permitting ocean simulations, which employs explicit viscous closures for momentum subgrid-scale fluxes paired with low-order oscillatory advection schemes. Our method is constructed with two objectives in mind: (i) ensuring stability through variance dissipation of both rotational and divergent motions, eliminating the need for additional explicit dissipation, and (ii) minimizing numerical diffusion through a novel approach to smoothness metrics in the WENO framework. The outcome is a method that delivers a higher “effective” resolution of the mesoscale turbulent spectra in eddy-permitting ocean simulations when compared to standard approaches. Figure 1 shows snapshots of the surface kinetic energy from a global ocean simulation run at the “eddy permitting” lateral resolution of 1/12th degree using the novel method. The solution is characterized by a rich web of well-resolved sharp jets without grid-scale noise. We will show that traditional explicit schemes generate much noisier solutions at the grid-scale at the same resolution.

The paper is organized as follows. In section 2 we derive the new formulation of the rotational advection operator that lends itself to an ILES discretization. In section 3, we describe the WENO reconstruction scheme and show how it can be applied to fluxed quantities in the context of the rotational form of the primitive equations. We test our newly defined WENO reconstruction in the context of two-dimensional decaying turbulence in section 4 and, finally, in section 5 we test the new rotational-based advection operator as a momentum closure alternative in an idealized baroclinic jet case. We conclude with some discussion in section 6.

¹ The Navier-Stokes equations under the hydrostatic approximation are referred to as the primitive equations in the atmospheric and ocean modeling literature.

2 An upwinding approach applied to the rotational form of the primitive equations

Ocean mesoscale turbulence is characterized by an inverse cascade of energy from small to large scales, weak energy dissipation, and a forward cascade of enstrophy terminated by enstrophy dissipation at small scales. Typical finite-volume discretizations of the primitive equations generate oscillatory noise at small scales that must be countered with explicit dissipation, typically via an empirical hyperviscosity. The objective of this section is to explore an alternative discretization of the primitive equations that is inherently diffusive and therefore does not generate oscillatory grid-scale noise. Specifically, we propose a discretization that effectively diffuses vorticity and horizontal divergence and leads to minimal energy dissipation by following principles (1)-(5) outlined in the previous section.

2.1 High-level description of the upwinding strategy

To provide an introductory sketch of our discretization, consider the rotational form of the advective terms in the horizontal momentum equations,

$$\partial_t u = + \underbrace{\zeta v}_{\text{vorticity flux}} - \underbrace{w \partial_z u}_{\text{vertical advection}} - \underbrace{\partial_x K}_{\text{kinetic energy gradient}} + \dots, \quad (1)$$

$$\partial_t v = - \underbrace{\zeta u}_{\text{vorticity flux}} - \underbrace{w \partial_z v}_{\text{vertical advection}} - \underbrace{\partial_y K}_{\text{kinetic energy gradient}} + \dots, \quad (2)$$

where u, v are the horizontal velocity components, $\zeta \stackrel{\text{def}}{=} \partial_x v - \partial_y u$ is the vertical vorticity, and $K \stackrel{\text{def}}{=} \frac{1}{2} (u^2 + v^2)$ is the horizontal kinetic energy. Mass conservation is enforced by the continuity equation for an incompressible fluid like seawater,

$$\underbrace{\partial_x u + \partial_y v}_{\stackrel{\text{def}}{=} d} = -\partial_z w, \quad (3)$$

where we have defined the horizontal divergence, d .

To lighten the notation we outline our discretization on a horizontally-isotropic rectilinear grid with regular horizontal spacing Δ . The discretization follows the staggered C-grid finite volume approach shown in [Appendix B](#). A simplified representation of the variables' relative location on the discrete grid is shown in figure 2.

We use the vorticity flux to exemplify the numerical error associated with the widely used momentum advection schemes in computational oceanography. An “enstrophy-conserving” ([Arakawa, 1966](#)) discretization on a C-grid requires the *reconstruction* of average vorticity at the velocity locations (see figure 2) where $\tilde{\zeta}_u$ and $\tilde{\zeta}_v$ express the *true* value of vorticity averaged in the volumes corresponding to velocity locations. Using a centered second-order approximation, denoted here with angle brackets:

$$\tilde{\zeta}_u \approx \langle \zeta \rangle^j \stackrel{\text{def}}{=} \frac{\zeta_{i,j+1} + \zeta_{i,j}}{2}, \text{ for use in } \zeta v, \quad (4)$$

$$\tilde{\zeta}_v \approx \langle \zeta \rangle^i \stackrel{\text{def}}{=} \frac{\zeta_{i+1,j} + \zeta_{i,j}}{2}, \text{ for use in } \zeta u. \quad (5)$$

We compute the numerical error \mathcal{N}_ζ by assuming that Δ is small and performing a Taylor expansion

$$\zeta_{i,j+1} = \tilde{\zeta}_u + \frac{\Delta}{2} \partial_y \zeta + \frac{\Delta^2}{8} \partial_y^2 \zeta + \mathcal{O}(\Delta^3), \quad (6)$$

$$\zeta_{i,j} = \tilde{\zeta}_u - \frac{\Delta}{2} \partial_y \zeta + \frac{\Delta^2}{8} \partial_y^2 \zeta - \mathcal{O}(\Delta^3), \quad (7)$$

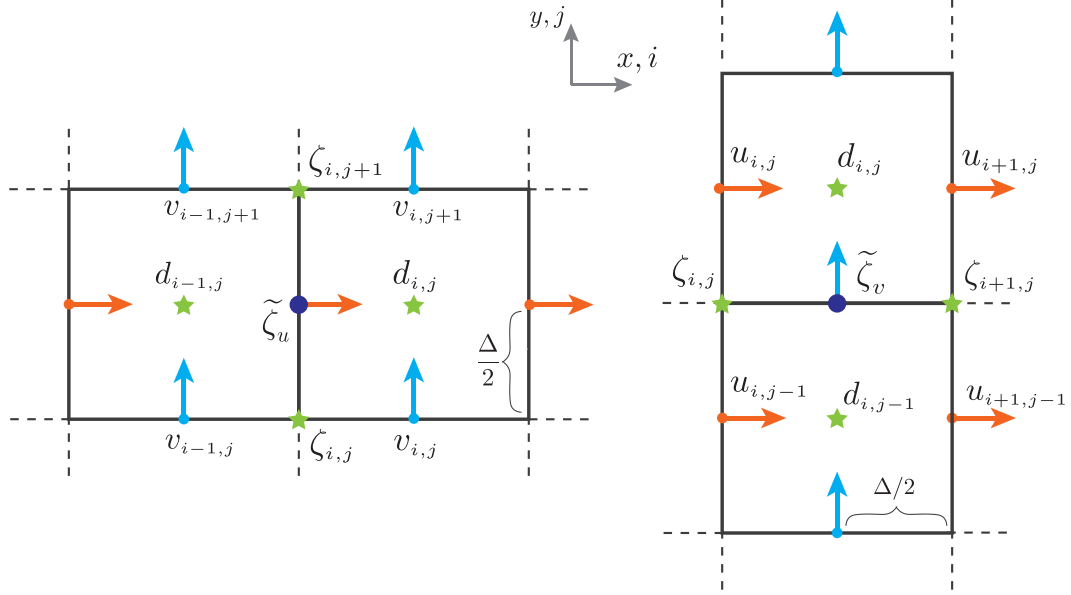


Figure 2. A sketch showing the variables' relative location on a staggered C-grid. Red and blue arrows denote the location of u - and v -velocity components, respectively; green stars show the location of vertical vorticity and horizontal divergence. Purple circles ($\tilde{\zeta}_u$ and $\tilde{\zeta}_v$) are the *average* vorticities required to calculate the vorticity flux at u locations (left) and at v locations (right).

where

$$\frac{\zeta_{i,j+1} + \zeta_{i,j}}{2} = \tilde{\zeta}_u + \mathcal{N}_\zeta, \quad \text{with} \quad \mathcal{N}_\zeta = \frac{\Delta^2}{8} \partial_y^2 \zeta + \mathcal{O}(\Delta^4). \quad (8)$$

In the same way, a centered discretization of the y -momentum vorticity flux leads to $\mathcal{N}_\zeta \sim \Delta^2 \partial_x^2 \zeta$ in (2). This truncation error is proportional to an even derivative of the vorticity field and therefore an odd derivative of the momentum field, acting as an additional spurious dispersion term in the momentum equations. By constructing $\partial_x(2) - \partial_y(1)$, we can see that the same error is dispersive also in the vorticity evolution equation and leads to additional numerical rotational modes.

The vorticity flux is not the only term that leads to dispersion, the same analysis (not done here) shows that a centered reconstruction of the vertical velocity in the vertical advection term leads to a numerical error that is proportional to the horizontal divergence

$$\mathcal{N}_d \sim \Delta^2 \int_0^z (\partial_x^2 d) dz \quad \text{in (1)}, \quad \text{and} \quad \mathcal{N}_d \sim \Delta^2 \int_0^z (\partial_y^2 d) dz \quad \text{in (2)}. \quad (9)$$

Here we have neglected the errors associated with the z -discretization as, in the primitive equations, numerical errors generated by the horizontal discretization are generally much larger than vertical ones.

We seek to improve the numerical error associated with vorticity reconstruction both by reducing its magnitude and also by computing the reconstruction so that the error is diffusive, and therefore “smooth”, rather than dispersive and “noisy”. For this we follow [Ringer \(2011\)](#), who proposed an upwind reconstruction of vorticity in the context of two-dimensional turbulence. Upwind reconstructions are diffusive: an upwind reconstruction of quantity a with respect to a velocity u leads to a truncation error that is proportional to $|u| \partial^n a$, with n an odd exponent equal to the upwinding order ([Norman et al., 2023](#)). The error of upwind vorticity reconstruction is proportional to an odd derivative of vorticity – hence an even derivative of the velocity field – and acts as a diffusion of momentum in the momentum equations:

$$\mathcal{N}_\zeta \sim \Delta^n |v| \partial_y^n \zeta \quad \text{in (1)}, \quad \mathcal{N}_\zeta \sim \Delta^n |u| \partial_x^n \zeta \quad \text{in (2)}. \quad (10)$$

This error will act diffusively also in the vorticity evolution equation as it is an even derivative of the vorticity, dissipating enstrophy in accordance with the forward enstrophy cascade characteristic of a two-dimensional flow.

Next, we turn to the vertical advection term. An upwind reconstruction of vertical advection in the rotational formulation is not achieved as easily as vorticity reconstruction or flux-form reconstruction (for example, as in Shchepetkin and McWilliams (1998b)), since the major source of dispersion is the advecting variable (w) rather than the vertical reconstruction of the advected quantity ($\partial_z u$). One of the major contributions of this work is to disentangle the dispersion related to the divergence field from a conservative vertical advection, by rewriting the vertical advection term using (3) such that

$$w\partial_z u = \underbrace{ud}_{\text{divergence flux}} + \underbrace{\partial_z(wu)}_{\text{conservative vertical advection}}, \quad (11)$$

$$w\partial_z v = \underbrace{vd}_{\text{divergence flux}} + \underbrace{\partial_z(wv)}_{\text{conservative vertical advection}}. \quad (12)$$

We have thus relegated the horizontal dispersive error, tied to the vertical velocity w , to a “divergence flux” term, akin to the vorticity flux. Contrary to the vertical advection terms in (1)–(2), the “divergence fluxes” in (11)–(12) are clearly amenable to an upwinding strategy. In particular, we use upwinded reconstruction of d with respect to u in ud term in (11), and vice versa upwinded reconstruction of d with respect to v in vd term in (12), which changes the dispersive error in (9) to

$$\mathcal{N}_d \sim \Delta^n |u| \partial_x^n d \text{ in (1), and } \mathcal{N}_d \sim \Delta^n |v| \partial_y^n d \text{ in (2).} \quad (13)$$

Deriving the horizontal divergence evolution equation $\partial_x(1) + \partial_y(2)$ shows that this approach leads to a direct diffusion of the horizontal divergence. This implementation allows a mitigation of the dispersion inherent in the vertical velocity field as it removes spurious numerical divergent modes similar to how vorticity upwinding removes spurious numerical rotational modes.

2.2 Detailed implementation in the discrete primitive equations

We concretize the approach explained above on an orthogonal C-grid, where the relevant metrics such as cell volumes ($\mathcal{V}_u, \mathcal{V}_v, \mathcal{V}_w$), facial areas ($\mathcal{A}_x, \mathcal{A}_y, \mathcal{A}_z$) and spacings ($\Delta_x, \Delta_y, \Delta_z$) are shown in figure B1. In addition to the angle bracket notations, we use double brackets and δ to express double centered reconstructions and finite differences, respectively:

$$\langle\langle a \rangle\rangle^{ij} \stackrel{\text{def}}{=} \left\langle \langle a \rangle^i \right\rangle^j, \quad \text{and} \quad \delta_i a \stackrel{\text{def}}{=} a_{i+1} - a_i. \quad (14)$$

Additionally, we use curly braces $\{ \cdot \}$ to indicate upwinding where $\{a\}^i$ denotes an upwind reconstruction of variable a in the x -direction with respect to the x -velocity component (u). The specific formulation of the upwind reconstruction we use in this paper will be shown in section 3.

We review here the centered-second order discretization schemes typically used in ocean modeling. We indicate the discrete counterpart to the vorticity flux, the vertical advection, and the kinetic energy gradient, with \mathcal{Z}, \mathcal{V} , and \mathcal{K} , respectively. We use subscripts u and v to denote the x -momentum and y -momentum components of the discrete terms. The “enstrophy conserving” centered second-order discretization of the vorticity flux term (Arakawa, 1966) in this notation is

$$\mathcal{Z}_u = \frac{\langle\langle \Delta_x v \rangle\rangle^{ij}}{\Delta_x} \langle \zeta \rangle^j, \quad \mathcal{Z}_v = \frac{\langle\langle \Delta_y u \rangle\rangle^{ij}}{\Delta_y} \langle \zeta \rangle^i. \quad (15)$$

\mathcal{K} is usually formulated as (Madec et al., 2022)

$$\mathcal{K}_u = \frac{\langle \delta_i u^2 \rangle^i + \langle \delta_i v^2 \rangle^j}{2\Delta_x}, \quad \mathcal{K}_v = \frac{\langle \delta_j u^2 \rangle^i + \langle \delta_j v^2 \rangle^j}{2\Delta_y}, \quad (16)$$

while the discrete vertical advection \mathcal{V} is derived from \mathcal{K} to ensure the following integral energy conservation property (Madec et al., 2022):

$$\sum_{i,j,k} (u \mathcal{V}_u \mathcal{V}_u + v \mathcal{V}_v \mathcal{V}_v) + \sum_{i,j,k} (u \mathcal{V}_u \mathcal{K}_u + v \mathcal{V}_v \mathcal{K}_v) = 0. \quad (17)$$

This property ensures that the change in discrete energy from the vertical advection term is balanced by the kinetic energy gradient. When paired with an energy-conserving vorticity flux implementation, the overall scheme conserves discrete energy in the system.

Following our approach, we implement an upwind reconstruction of vorticity in (15) by substituting the following terms

$$\langle \zeta \rangle^i \mapsto \{\zeta\}^i \text{ and } \langle \zeta \rangle^j \mapsto \{\zeta\}^j. \quad (18)$$

To derive a suitable discrete form for the conservative vertical advection and the divergence flux (which we denote \mathcal{C} and \mathcal{D}), we manipulate \mathcal{V} to ensure discrete energy conservation through

$$\sum_{i,j,k} (u \mathcal{V}_u \mathcal{V}_u + v \mathcal{V}_v \mathcal{V}_v) = \sum_{i,j,k} [u \mathcal{V}_u (\mathcal{C}_u + \mathcal{D}_u) + v \mathcal{V}_v (\mathcal{C}_v + \mathcal{D}_v)]. \quad (19)$$

The derivation is performed in [Appendix C](#). The resulting discrete formulations read

$$\mathcal{C}_u = \frac{\delta_k \langle W \rangle^i \langle u \rangle^k}{\mathcal{V}_u}, \quad \mathcal{C}_v = \frac{\delta_k \langle W \rangle^j \langle v \rangle^k}{\mathcal{V}_v}, \quad (20)$$

$$\mathcal{D}_u = \frac{u \langle D \rangle^i}{\mathcal{V}_u}, \quad \mathcal{D}_v = \frac{v \langle D \rangle^j}{\mathcal{V}_v}, \quad (21)$$

where $D = \delta_i U + \delta_j V$ is the discrete horizontal divergence, $U = \mathcal{A}_x u$, $V = \mathcal{A}_y v$, and $W = \mathcal{A}_z w$. As done in (18), upwind reconstruction in \mathcal{C} and \mathcal{D} is ensured by

$$\langle u \rangle^k \mapsto \{u\}^k \text{ and } \langle v \rangle^k \mapsto \{v\}^k, \quad (22)$$

$$\langle D \rangle^i \mapsto \{D\}^i \text{ and } \langle D \rangle^j \mapsto \{D\}^j. \quad (23)$$

As we show in [Appendix D](#), numerical errors that scale with a cross-derivative of the velocity field can lead to grid-scale energy generation instead of energy dissipation. For example, since $d = \partial_x u + \partial_y v$, a straightforward first-order upwind reconstruction of d in the x -direction leads to

$$\mathcal{N}_d \sim |u|(\partial_x^2 u + \partial_x \partial_y v), \quad (24)$$

where $\partial_x^2 u$ is diffusive while $\partial_x \partial_y v$ has the potential to be anti-diffusive. The opposite happens in the y -direction. To avoid injecting energy at the grid scale, we define the upwind reconstruction of the discrete divergence as a reconstruction that guarantees discrete energy dissipation. For this reason, we implement upwinding of D as follows

$$\{D\}^i \stackrel{\text{def}}{=} \{\delta_i U\}^i + \langle \delta_j V \rangle^i, \quad (25)$$

$$\{D\}^j \stackrel{\text{def}}{=} \langle \delta_i U \rangle^j + \{\delta_j V\}^j. \quad (26)$$

We follow the same implementation for \mathcal{K} , where we recognize the similarity between \mathcal{D} and \mathcal{K} ($u \partial_x u = \frac{1}{2} \partial_x u^2$ and $v \partial_y v = \frac{1}{2} \partial_y v^2$) and can safely substitute

$$\langle \delta_i u^2 \rangle^i \mapsto \{\delta_i u^2\}^i \text{ and } \langle \delta_j v^2 \rangle^j \mapsto \{\delta_j v^2\}^j, \quad (27)$$

in equation (16).

The approach we sketched results in an “ILES-inspired” method that is energetically dissipative, tackles stability issues through an upwinding strategy, and removes grid-scale variance when applied to the rotational form of the primitive equations. The main ingredients are the splitting of the vertical advection term (11)-(12), the discrete energy conserving implementation (20)-(21) followed by the targeted upwind substitutions (18), (22), (23), and (27). We have not yet described how to perform the upwinding, which, in principle, can be done with any diffusive reconstruction scheme. In the next section, we propose an optimal WENO-based reconstruction that pairs with the discretization detailed above and allows a minimal level of energy dissipation.

3 WENO reconstruction scheme for the rotational primitive equations

The Weighted Essentially Non-Oscillatory (WENO) scheme is a particular implementation of the Essentially Non-Oscillatory schemes first introduced by [Harten et al. \(1987\)](#) and refined by [Shu \(1997\)](#). The WENO scheme is especially appropriate to resolve shocks that develop in solutions of partial differential equations such as the Euler equations or the shallow water equations. The central idea behind the WENO scheme is to dynamically approximate a numerical flux with multiple low-order reconstructing polynomials. These polynomials are combined using nonlinear weights that depend on the smoothness of each individual polynomial, with the objective of obtaining a high-order upwind reconstruction in smooth regions and lower-order upwind reconstruction in regions where the solution is less smooth. This approach allows the scheme to achieve high accuracy even in regions of high gradients and discontinuities while, at the same time, avoiding artificial oscillations (dispersive artifacts) that plague conventional high-order methods.

We start by reviewing the mathematical implementation of a WENO reconstruction. Given a discrete quantity ϕ , we denote with $[\phi]_r^i$ the one-dimensional reconstruction obtained by the r -th candidate polynomial of order s ($p_{r\phi}$ for $r \in \{0, \dots, s-1\}$) in the i -th direction, that is:

$$[\phi]_r^i \stackrel{\text{def}}{=} p_{r\phi}(x_{i+1/2}) = \sum_{j=0}^{s-1} c_{rj} \phi_{i-r+j}, \quad \text{with } r \in \{0, \dots, s-1\}. \quad (28)$$

c_{rj} are linear reconstructing weights and $x_{i+1/2}$ is the final x position of $[\phi]_r^i$ on the discrete grid ([Shu, 1997](#)). The WENO reconstruction procedure is a convex combination of the candidate reconstructions and is implemented as follows:

$$\{\phi\}^i = \sum_{r=0}^{s-1} \xi_{r\phi} [\phi]_r^i, \quad \text{with } \xi_{r\phi} = \frac{\alpha_{r\phi}}{\sum_{r=0}^{s-1} \alpha_{r\phi}} \quad \text{and } \alpha_{r\phi} = f(\alpha_r^*, \beta_{r\phi}). \quad (29)$$

Above, ξ_r are the nonlinear WENO weights, which are functions of the optimal linear weights (α_r^*) weighted by a measure of smoothness of the field $\beta_{r\phi}$, where the subscript ϕ indicates that β is calculated from field ϕ . The α_r^* optimal linear weights are obtained by equating the final reconstruction $\{\phi\}^i$ to a classical upwind biased reconstruction of order $2s-1$ when the field ϕ is smooth ($\beta_{r\phi} = 0$ for each $r \in \{0, \dots, s-1\}$). Several formulations for smoothness weighting (f) have been put forth, and, while the exact formulation of the α weights is not a central concern of this work, it is noteworthy to mention that we employ the WENO-Z formulation ([Balsara & Shu, 2000](#)). In terms of smoothness indicators, the most widespread approach is to use a Sobolev norm of the reconstructing polynomial $p_{r\phi}$ over the interval $(x_{i-1/2}, x_{i+1/2})$ ([Shu, 1997](#)):

$$\beta_{r\phi} \stackrel{\text{def}}{=} \sum_{\ell=1}^{s-1} \int_{x_{i-1/2}}^{x_{i+1/2}} \Delta x^{2\ell-1} (\partial_x^\ell p_{r\phi})^2 dx. \quad (30)$$

For “flux-form” advection, the reconstructed field is typically the same as the field that is advanced in time. As such, using ϕ to compute β_r , directly connects the smoothness

evaluation to the evolved quantity. This is not the case in the rotational form of the Navier–Stokes equations where the field evolved in time is typically not the same as the field being reconstructed. Specifically, in the derivation outlined in the preceding section, upwind reconstruction is applied to six distinct quantities:

$$\{\zeta\}^i, \{u\}^k, \{D\}^i, \{\delta_i u^2\}^i \quad \text{in the } u \text{ evolution equation,} \quad (31)$$

$$\{\zeta\}^j, \{v\}^k, \{D\}^j, \{\delta_j v^2\}^j \quad \text{in the } v \text{ evolution equation.} \quad (32)$$

Many terms in (31)–(32) above involve derivatives of the velocities and thus exhibit rapid variations at the grid scale compared to the dynamics of the horizontal momentum fields. In this context, we found that $\beta_{r\phi}$ is an inadequate smoothness measure since it lacks an intuitive connection with the dynamics of the evolved field – specifically, the velocity field, which is significantly smoother than the upwinded quantities. Due to this discrepancy, $\beta_{r\phi}$ in (29) causes an artificial decrease of the WENO reconstruction order leading to a larger-than-necessary dissipation. We demonstrate this in section 4 within the context of two-dimensional decaying turbulence.

Based on the above discussion, we propose here an alternative approach to assess smoothness, wherein we employ the reconstructing polynomials of a “parent” (smoother) field constructed directly from velocities, rather than from their derivatives. An exception is the divergence flux: we find that the divergence flux term contributes the most to grid-scale noise and, as such, we choose to diffuse it consistently with its intrinsic smoothness. We introduce notation to facilitate the description and understanding of our approach. In this notation, a WENO reconstruction is denoted as

$$\{\phi; \psi\}, \quad (33)$$

where ϕ represents the field being reconstructed and ψ is the field used for assessing the smoothness. Under the conventional WENO scheme, where the reconstructed and smoothness-diagnosed fields are identical, this notation simplifies to $\{\phi; \phi\}$. We use the notation $\{\phi; \psi\}^i$ as short-hand for the following reconstruction

$$\{\phi; \psi\}^i = \sum_{r=0}^{s-1} \xi_{r\psi} [\phi]_r^i, \quad \text{with } \beta_{r\psi} \stackrel{\text{def}}{=} \sum_{\ell=1}^{s-1} \int_{x_{i-1/2}}^{x_{i+1/2}} \Delta x^{2\ell-1} (\partial_x^\ell p_{r\psi})^2 dx, \quad (34)$$

where $p_{r\psi}$ is the reconstructing polynomial of quantity ψ .

The smoothness-optimized upwind WENO reconstructions, written in the above-presented notation, are

$$\{\zeta; \mathbf{u}\}^i, \{u; u\}^k, \{D; D\}^i, \left\{ \delta_i u^2; \langle u \rangle^i \right\}^i \quad \text{in the } u \text{ evolution equation,} \quad (35)$$

$$\{\zeta; \mathbf{u}\}^j, \{v; v\}^k, \{D; D\}^j, \left\{ \delta_j v^2; \langle v \rangle^j \right\}^j \quad \text{in the } v \text{ evolution equation,} \quad (36)$$

where we define the upwinding of ζ as an average between a u -based and a v -based reconstruction:

$$\{\zeta; \mathbf{u}\} \stackrel{\text{def}}{=} \frac{\left\{ \zeta; \langle u \rangle^j \right\} + \left\{ \zeta; \langle v \rangle^i \right\}}{2}. \quad (37)$$

Using reconstructed variables $\langle v \rangle$ and $\langle u \rangle$ as smoothness metrics and not u and v directly is a consequence of the staggered C-grid discretization. The final implementation of the discrete primitive equations following our ILES approach is detailed in Appendix B.

4 Two-dimensional homogeneous decaying turbulence test case

We assess our new ILES method first through simulations of decaying two-dimensional homogeneous turbulence. The purpose of this test is to compare the ILES approach with a

Table 1. Description of test cases

Name	Legend	Vorticity Flux	Vorticity smoothness	SGS closure
DNS	—	Energy conserving	—	—
Leith1	---	Energy conserving	—	Leith, $\mathbb{C} = 1$
Leith2	—	Energy conserving	—	Leith, $\mathbb{C} = 2$
W5D	---	WENO 5th order	$\{\zeta; \zeta\}$	—
W9D	—	WENO 9th order	$\{\zeta; \zeta\}$	—
W5V	---	WENO 5th order	$\{\zeta; \mathbf{u}\}$	—
W9V	—	WENO 9th order	$\{\zeta; \mathbf{u}\}$	—

state-of-the-art explicit closure in a setting where it is computationally feasible to run Direct Numerical Simulations (DNS), i.e. simulations that resolve scales down to dissipation. The DNS will be considered the ground truth and used to assess the skill of ILES at coarser resolution.

We further assess the impact of decoupling the reconstruction polynomials from the smoothness assessment by performing ILES using both $\{\zeta; \mathbf{u}\}$ and $\{\zeta; \zeta\}$. Since divergent motions are absent in a two-dimensional setting, this test case is best suited to assess the discrete properties of the vorticity flux reconstruction.

We solve the incompressible two-dimensional Navier–Stokes equations in non-dimensional form, i.e.,

$$\partial_t \mathbf{u} + \zeta \hat{\mathbf{k}} \times \mathbf{u} = -\nabla(p + K) + \frac{1}{Re} \nabla^2 \mathbf{u} + \nabla \cdot \boldsymbol{\tau}_{\text{SGS}}, \quad (38)$$

$$\nabla \cdot \mathbf{u} = 0. \quad (39)$$

Notice that \mathbf{u} and ∇ denote the two-dimensional rather than the three-dimensional velocity vector and gradient in this section. The simulations are run with a $Re = 3.3 \times 10^4$ on a doubly periodic box of nondimensional size $2\pi \times 2\pi$.

We initialize the simulations with velocities generated through a narrow-band energy spectrum as proposed by Ishiko et al. (2009),

$$E(k) = \frac{1}{2} a_s k_p^{-1} \left(\frac{k}{k_p} \right)^7 \exp \left[-\frac{7}{2} \left(\frac{k}{k_p} \right)^2 \right], \quad (40)$$

where $k \stackrel{\text{def}}{=} (k_x^2 + k_y^2)^{1/2}$ is the magnitude of the wavenumber vector, $a_s = 16/3$, and $k_p = 12$ is the wavenumber corresponding to maximum energy. With this choice of initial condition and Reynolds number, we achieve a good spectral separation between the energy-containing and dissipation scales. To construct a velocity field with this energy spectrum, we first generate a vorticity field in Fourier space

$$\hat{\zeta}(k_x, k_y) = \left[\frac{k}{\pi} E(k) \right]^{1/2} e^{i\phi(k_x, k_y)}, \quad (41)$$

where $\phi(k_x, k_y)$ are random phases chosen such that the vorticity field in physical space is real (Ishiko et al., 2009). The initial velocity distributions are then given by:

$$\hat{u}(k_x, k_y) = \frac{ik_y}{k^2} \hat{\zeta}(k_x, k_y), \quad \hat{v}(k_x, k_y) = -\frac{ik_x}{k^2} \hat{\zeta}(k_x, k_y). \quad (42)$$

The simulations are run for $t = 6$ nondimensional time units.

The fully resolved benchmark solution employs the second-order energy-conserving advection discretization, as per Eq. (D4) and $N = 4096 \times 4096$ grid points. We compare it with solutions obtained using coarser grids and three distinct SGS methods. The first,

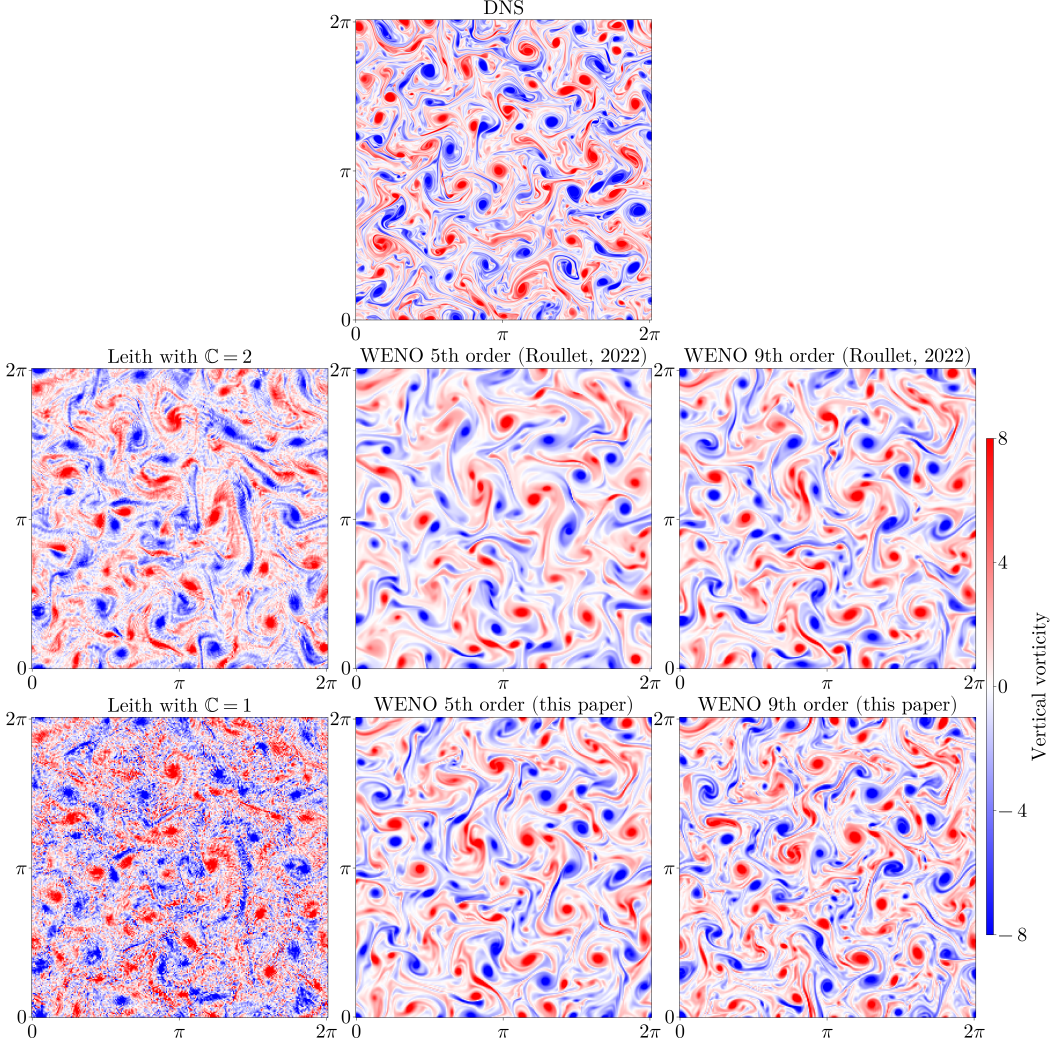


Figure 3. Vorticity at $t = 3.6$ after initialization. Comparison between DNS (top panel), explicit LES with a Leith viscosity (left panels), and implicit LES with a rotational WENO discretization with $N = 256^2$. Of the WENO schemes, the top panels show the results obtained with a standard WENO reconstruction of vorticity $\{\zeta; \zeta\}$ (W5D and W9D in table 1) while the bottom panels show a reconstruction using the velocity field as smoothness measure $\{\zeta; \mathbf{u}\}$ (W5V and W9V in table 1).

deemed the current best practice, is a second-order energy-conserving advection operator together with the Leith closure (see Appendix A). We do not consider the adaptive Leith scheme, because it is too expensive for oceanographic applications. Instead, we consider the traditional Leith scheme for two different values of the nondimensional parameter \mathbb{C} : $\mathbb{C} = 1$ and $\mathbb{C} = 2$. The second method involves the rotational WENO, using standard smoothness diagnosis $\{\zeta; \zeta\}$ as in the work by Roulet and Gaillard (2022). The third method employs the new rotational WENO, where vorticity is reconstructed as $\{\zeta; \mathbf{u}\}$. For the WENO schemes we compare fifth- and a ninth-order reconstruction schemes. All the different methods are summarized in table 1.

The grid size for the under-resolved simulations is ramped up from 64×64 , where only the largest structures are resolved, to 128×128 , 256×256 , and finally 1024×1024 , where the grid is fine enough to resolve most of the energy and enstrophy spectra. For reference, in a high-resolution global ocean simulation, the grid barely resolves the largest-scale eddies and is therefore more similar to the 64×64 or 128×128 case than the 1024×1024 .

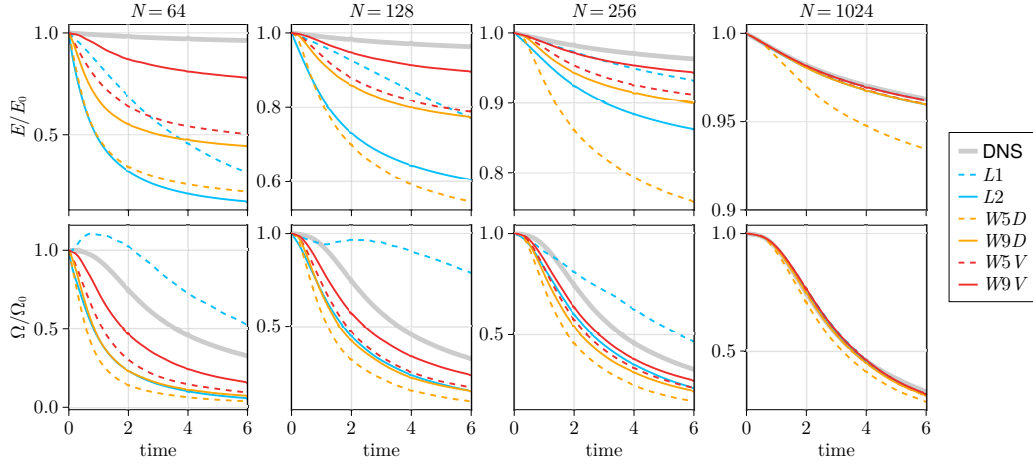


Figure 4. Evolution in time of integrated kinetic energy (top row) and integrated enstrophy (bottom row). Advection schemes and numerical details are shown in table 1.

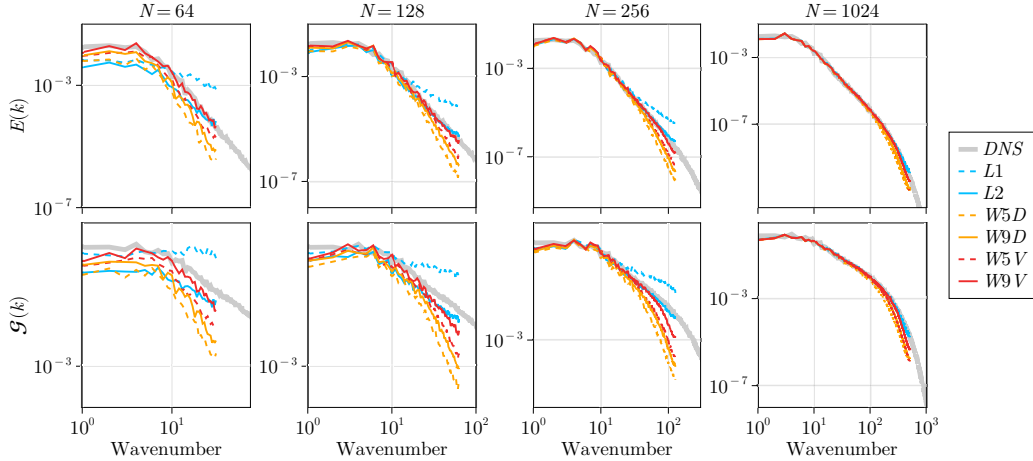


Figure 5. Kinetic energy spectra (top panels) and enstrophy spectra (bottom panels) at $t = 3.6$. Advection schemes and numerical details are shown in table 1.

Figure 3 shows a comparison of the vertical vorticity at $t = 3.6$. The top panel shows the DNS solution, while the center and bottom panels show the under-resolved simulations. The Leith closure, even when using the larger parameter $C = 2$, results in substantial nonphysical noise at the grid scale. We conclude that for this problem, the Leith closure fails to uphold principle (3) of a good SGS closure. In contrast, all ILES based on WENO reconstructions yield a turbulent solution completely devoid of grid-scale noise.

Figure 4 illustrates the evolution of kinetic energy (top panels) and enstrophy (bottom panels) for the various methods at different resolutions. The evolution of both quantities converges to the DNS solution at 1024×1024 for all methods as the resolution is increased, except for the WENO fifth-order with standard vorticity reconstruction (W5D) which exhibits excessive energy dissipation. This scheme fails to uphold principle (1) of an effective SGS closure. As for the Leith closures, they do converge to the DNS solution at the highest resolution (1024×1024) but are severely deficient at coarser resolutions. With $C = 1$, the solutions have too large enstrophy as the closure fails to remove grid-scale vorticity stemming from the centered advection scheme. With $C = 2$ the enstrophy levels are reduced, but at the cost of too low kinetic energy. The difference between $C = 1$ and $C = 2$ illustrates

the fundamental challenge with explicit SGS closures combined with dispersive advective methods: removing spurious dispersive artifacts requires excessively high dissipation levels. Conversely, the WENO reconstruction schemes are designed to limit dispersive artifacts. Figure 4 shows that, as expected, the accuracy of the WENO approach increases with a higher discretization order. Most importantly the smoothness measure obtained with the new stencils $\{\zeta; \mathbf{u}\}$ achieves a higher effective resolution, i.e. converges faster to the DNS solution.

Figure 5 shows the energy (top panels) and enstrophy (bottom panels) spectra at $t = 3.6$. Again, all methods converge to the DNS solution at 1024×1024 (in the inertial range), except for the W5D case. At lower resolutions, the Leith closure with $C = 1$ fails to match the DNS spectra and exhibits a pile-up of variance at small scales. Using a larger parameter ($C = 2$) reduces the bias in small-scale variance at the expense of excessive damping of energy, especially at large scales; this is hard to appreciate in Fig. 5 because of the logarithmic scale, but is clear in Fig. 4. WENO reconstructions do overly dissipate enstrophy at small scales, as they are designed to do, but the energy spectra are much better captured especially with the $\{\zeta; \mathbf{u}\}$ reconstruction. This is vindication that the upwinding of vorticity dissipates enstrophy, but not energy, at small scales. In this case, a ninth-order WENO reconstruction of vorticity, using $\{\zeta; \mathbf{u}\}$ stencils (W9V), captures the DNS energy spectrum at all resolutions, down to 64×64 .

In conclusion, the explicit Leith closure accurately represents the DNS solution only at the highest resolution but fails at lower resolutions. This failure stems from the oscillatory dynamics of the centered advection scheme that produce grid-scale noise which is not selectively damped by the Leith closure. In practice, the closure results in either too much enstrophy at small scales or too little energy at all scales depending on parameter choices. In contrast, a WENO reconstruction of vorticity using $\{\zeta; \mathbf{u}\}$ dissipates enstrophy at small scales and preserves an accurate energy spectrum at all scales. Therefore, we deem the W9V approach more in line with the LES principles outlined in the introduction when compared to the other methods explored in this section.

5 Baroclinic jet test case

Next, we test our ILES approach using WENO reconstruction in a baroclinic jet setup. The setup consists of a periodic channel in a spherical sector between 60°S - 40°S , 20 degrees wide, and one kilometer deep. The simulations is initialized with a constant vertical stratification $N^2 = 4 \times 10^{-6} \text{ s}^{-2}$ and a meridional buoyancy front given by:

$$b(\phi, z) = N^2 z + \Delta b \begin{cases} 0 & \text{if } \gamma(\phi) < 0, \\ [\gamma(\phi) - \sin \gamma(\phi) \cos \gamma(\phi)]/\pi & \text{if } 0 \leq \gamma(\phi) \leq \pi, \\ 1 & \text{if } \pi < \gamma(\phi), \end{cases} \quad (43)$$

$$\gamma(\phi) = \frac{\pi}{2} - 2\pi \frac{\phi - \phi_0}{\Delta\phi}, \quad (44)$$

where $\phi_0 = 50^\circ\text{S}$ is the central latitude of the domain, $\Delta\phi = 20^\circ$ the domain's latitudinal extent, $\Delta b = 5 \times 10^{-3} \text{ m s}^{-2}$. The initial velocity is in thermal-wind balance with the buoyancy field and vanishes at $z = -H$. Thus the initial conditions are an equilibrium solution to the primitive equations, but one that is unstable to the development of baroclinic instability (Vallis, 2017).

The initial buoyancy and velocity profiles are shown in figure 6. We also add a weak white noise to the initial buoyancy profile to kick-start the baroclinic instability (not shown in the figure). We impose no-flux and free-slip boundary conditions on all solid walls. We also prescribe a background vertical viscosity $\nu = 10^{-4} \text{ m}^2 \text{s}^{-1}$ and a vertical diffusivity $\kappa = 10^{-5} \text{ m}^2 \text{s}^{-1}$ to account for vertical mixing. To sustain turbulence and allow an equilibrated solution, we linearly restore the zonally averaged buoyancy and velocity to the initial profiles with a timescale of 50 days (in a similar manner as done by Soufflet et al.

Table 2. Details of the two different methods. Both methods are tested on a 14 km, 7 km, and 3.5 km resolution.

Method Name	QG2	W9V
Vorticity flux (\mathcal{Z})	Energy conserving (B1)	WENO 9th order (B3)
Vertical advection (\mathcal{V})	Centered 2nd order (B2)	—
Divergence flux (\mathcal{D})	—	WENO 9th order (B5)
Conservative vertical advection (\mathcal{C})	—	WENO 5th order (B4)
Kinetic energy gradient (\mathcal{K})	Centered 2nd order (16)	WENO 5th order (B6)
Subgrid-scale closure	QGLEith with $C = 1$	—
Tracer advection	WENO 7th order	WENO 7th order

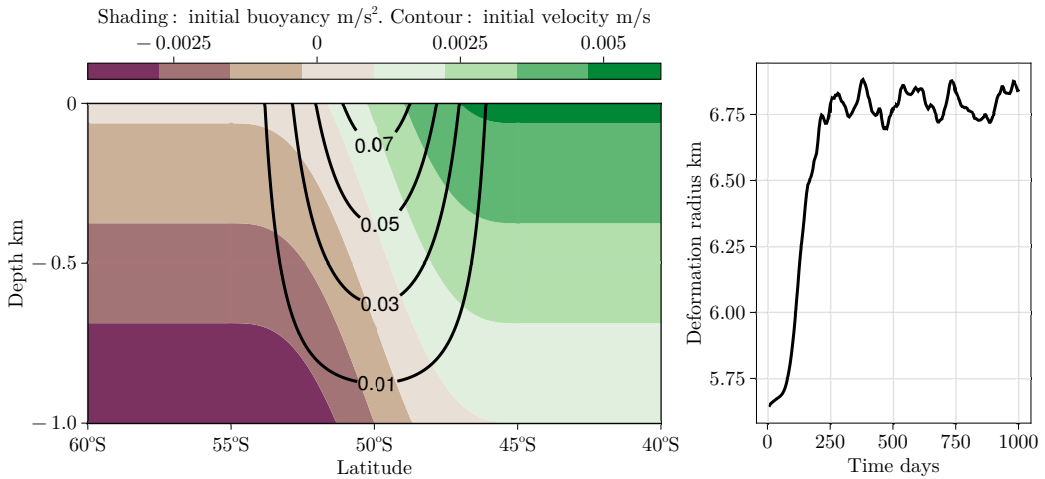


Figure 6. Left: The initial conditions (43): buoyancy (shading) and zonal velocity (contours). Right: The evolution of the domain-average deformation radius for the W9V case at 7km resolution.

(2016)). This restoring sets the zonal transport without interfering with the development of mesoscale eddies, which are the focus of this test. We run the simulations for a total of 1000 days.

We run two sets of simulations with different closures. One set uses the ninth-order WENO reconstruction of vorticity (\mathcal{Z}) and horizontal divergence (\mathcal{D}). We use a lower for \mathcal{C} and \mathcal{K} (5th order) as the order of these terms does not have a discernible effect on the solutions. On the other hand, a higher order in vorticity flux is less dissipative and allows a higher energy in the solution given that, in this setup, most energy is confined in rotational motions. The other set uses a second-order energy-conserving advection scheme with an explicit QGLEith closure (QG2), a quasi-geostrophic counterpart to the two-dimensional Leith closure which is used in ocean models (Appendix A). Tracer advection is more expensive than momentum advection in this case given the three-dimensional nature of the scheme when compared to the two-dimensional vorticity flux. We find that a 7th-order tracer advection scheme is a good compromise between efficiency and accuracy, and for this reason, we use a 7th-order WENO scheme for buoyancy advection in both sets. The numerical details for each simulation are summarized in table 2. Each set consists of three simulations run with horizontal resolutions of 1/8th, 1/16th, and 1/32nd of a degree, equivalent to a maximum (meridional) grid spacing of 14 km, 7 km, and 3.5 km, respectively. The vertical grid spacing is fixed at 20 meters.

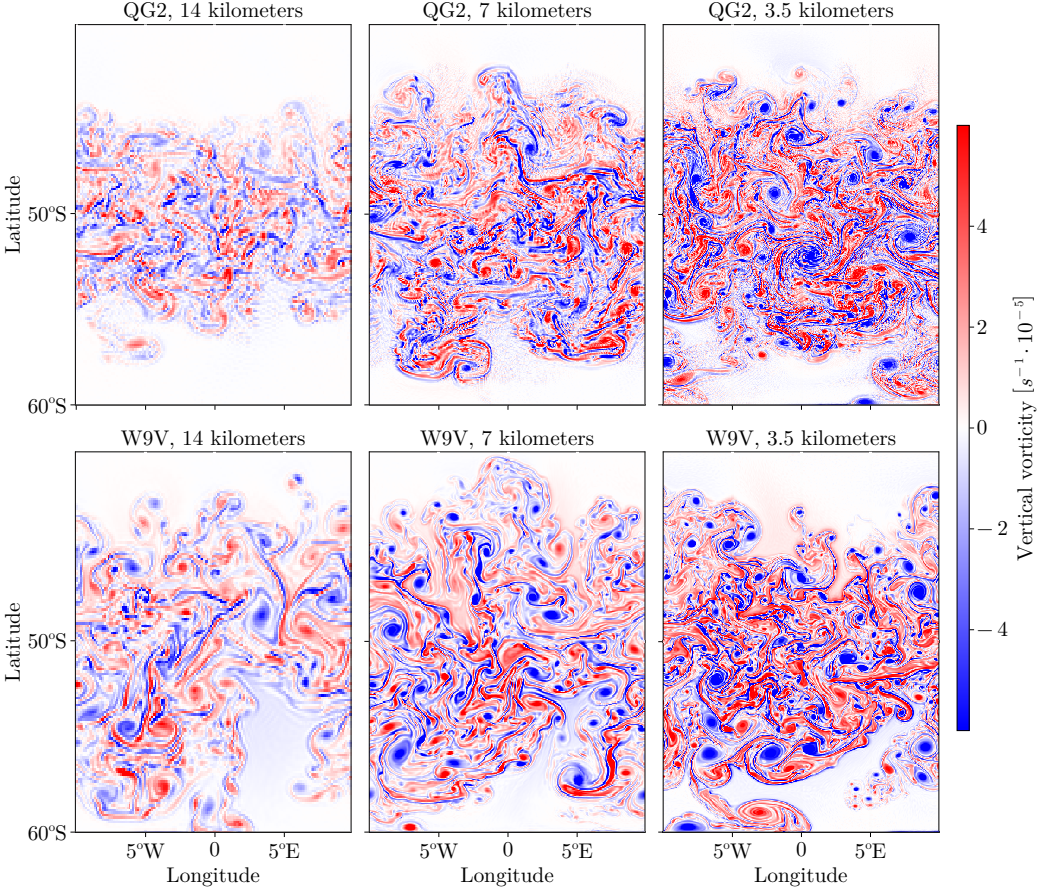


Figure 7. Near-surface vorticity for QG2 (top panels) and W9V (bottom panels) at 14, 7, and 3.5-kilometer resolution during the initial instability phase (day 200).

The baroclinic jet undergoes an initial baroclinic instability that develops into a statistically steady state around the 250th day, when the eddy kinetic energy dissipation balances the injection of potential energy generated by the buoyancy restoring. The most unstable mode of a baroclinically unstable jet is close to the deformation radius defined as (Vallis, 2017):

$$L_d \stackrel{\text{def}}{=} \frac{1}{\pi|f|} \int_{-H}^0 (\partial_z b)^{1/2} dz . \quad (45)$$

A fully resolved simulation requires a horizontal spacing finer than L_d . An eddy-permitting solution instead would have a grid size of the same order as the deformation radius (10-50 km in the ocean). In this baroclinic jet setup, the initial deformation radius is 5.5 km and adjusts to an equilibrium value of about 6.75 km as shown in figure 6. Thus, the highest resolution simulations are barely “resolved” with slightly more than one grid cell per deformation radius, while the 14 km tests are “under-resolved”. The 7-kilometer simulations are in a dynamical regime representative of typical eddy-permitting ocean models, which are run with a horizontal spacing between 10-20 km.

Figure 7 shows surface vorticity for the QG2 and W9V cases at different resolutions during the initial transient (day 200th). As resolution increases, eddy activity spreads to higher and lower latitudes, indicating that the frontal slumping has extended further in the domain. Additionally, the WENO solution shows a large spread of vorticity even in the 14 km case where the deformation radius is severely under-resolved. As in the two-dimensional test case, the explicit closure paired with an oscillatory advection scheme, results in substantial noise, visible by eye, which persists up to the highest resolution.

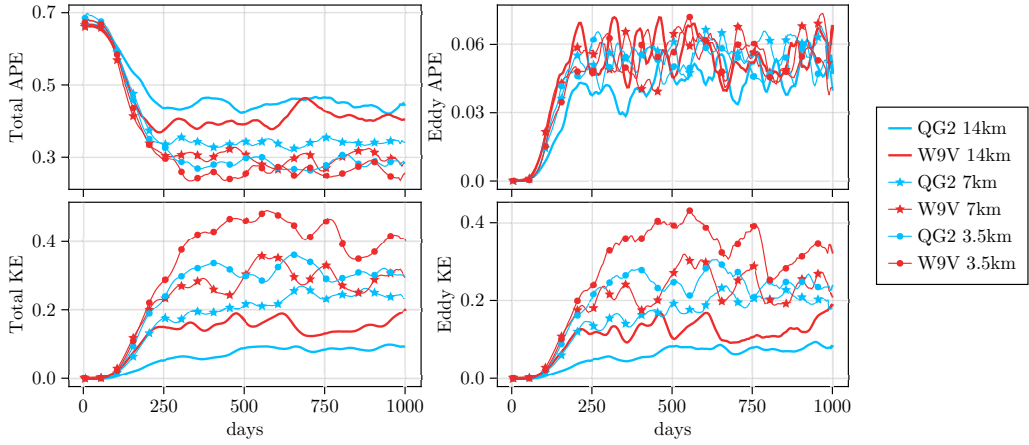


Figure 8. Timeseries of the integrated available potential energy (top panels) and kinetic energy (bottom panels). The left-hand side shows total variables while the right-hand side shows eddy quantities defined as a deviation from the instantaneous zonal mean.

The time series of total and eddy available potential energy (APE) and kinetic energy (KE) are shown in Figure 8. As expected, increasing resolution results in more APE conversion to EKE. The initial decrease of APE and increase of eddy KE depends on the instability timescale that converges at 7-kilometer resolution for W9V, but not for QG2. Indeed the timescale of the initial transient for the W9V case at 14-kilometer resolution matches the QG2 case at double the resolution. The transformation of mean APE to eddy KE occurs through conversion to eddy APE by means of baroclinic instability ($v'b' \partial_y b/N^2$), that is then converted to EKE through the vertical eddy flux ($w'b'$). Eddy available potential energy and eddy kinetic energy are further removed from the system by (mostly) numerical and physical dissipation. The much larger EKE in the W9V cases when compared to the QG2 counterparts suggests that the implicit dissipation intrinsic in the W9V scheme is significantly lower than the (explicit) energy dissipation provided by the QG2 subgrid-scale closure. Note that it is always possible to increase the eddy kinetic energy in the QG2 case by lowering the C parameter. But, as already stated in section 4 for the Leith case, this would exacerbate the already large grid-scale dispersion of vorticity. For this reason, calibrating C to achieve the low dissipation paired with grid-scale variance removal obtained in the W9V case is challenging.

To judge the “effective” resolution of the two approaches we look at zonal mean buoyancy averaged between 250 and 1000 days. The final buoyancy slope is determined by a balance between the mean buoyancy restoring, forcing the system towards the initial low-stratification jet state, and mesoscale eddies which tend to restratify the system. We expect a larger stratification for cases that are able to maintain higher levels of eddy kinetic energy as the equilibrium is pushed toward a lower APE state. Figure 9 shows mean buoyancy contours for the different cases where the filled contours show the QG2 case at 3.5-kilometer resolution. Figure 9 shows that, indeed, an increase in resolution leads to a more strongly stratified buoyancy profile, with W9V having a larger stratification than QG2, in virtue of the larger EKE expressed by the model. Notably, the W9V buoyancy contours at 7-kilometer resolution are practically indistinguishable from the buoyancy contours of the QG2 3.5-kilometer resolution, suggesting a similarly resolved mesoscale eddy field. Stratification for the W9V case at 3.5-kilometer resolution (not shown), is slightly larger than the QG2 case at 3.5-kilometer resolution indicating that convergence is still not achieved at 3.5 kilometers. However, convergence in this case is not expected, given that the deformation radius is only 6.75 kilometers. Achieving full conversion at this resolution would probably require a representation of the inverse energy cascade through a backscattering parameterization.

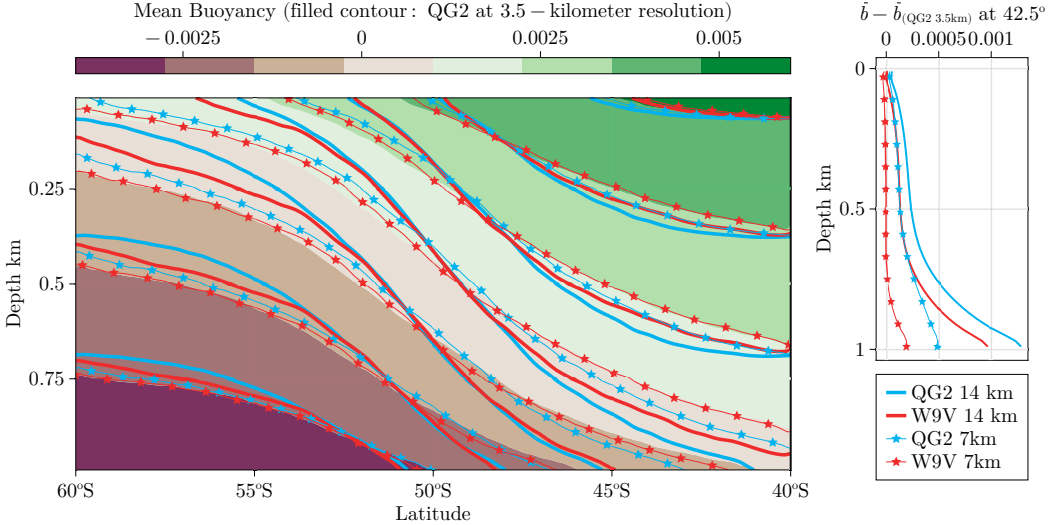


Figure 9. Left: Time and zonally averaged buoyancy for the different cases. The filled contour shows the results from the QG2 case at 3.5-kilometer resolution, acting as a reference. Right: deviation of the mean buoyancy from the QG2 case at 3.5-kilometer resolution. Note the higher resolution power of W9V when compared to QG2.

This test case in a more complex mesoscale turbulence simulation confirms that the W9V method achieves a higher “effective” resolution and less noisy solution than the QG2 method.

6 Summary and Conclusions

We introduced a new momentum advection scheme for the rotational form of the primitive equation based on the WENO reconstruction of fluxed variables (vorticity, horizontal divergence, and kinetic energy gradient). We constructed the new momentum advection scheme as an alternative to using explicit viscous closures for momentum subgrid-scale fluxes, with the rationale of performing “implicit” large eddy simulation of ocean turbulence. This is possible assuming that the effect of subgrid-scale turbulence on large scales is included implicitly in the diffusive reconstruction of transported quantities. We achieved this by (i) rewriting the primitive equations to expose both vorticity and horizontal divergence, (ii) implementing a diffusive reconstruction of fluxed variables (vorticity, horizontal divergence, and kinetic energy gradient), and (iii) choosing smoothness indicators for the WENO scheme that allow a minimally dissipative reconstruction.

We assessed the skill of this approach under four different principles: (1) convergence, (2) flow-awareness, (3) variance removal at the grid scale, and (4) adjustment to varying resolution. We found that our proposed approach outperforms the routinely used Leith closure in decaying homogeneous two-dimensional turbulence across a broader range of resolutions. Our method also outperformed QGLEith, a standard oceanographic approach based on explicit viscous dissipation paired with low-order momentum advection, in mesoscale turbulence simulations. Most importantly, our method does not require any calibration of unknown coefficients but rather it adjusts to varying resolutions and attains a superior “scale-awareness” when compared to diffusive viscous closures typically used in climate models. In addition to this scale awareness, our novel scheme achieves minimal dissipation, while efficiently removing variance at the grid-scale. Thus solutions obtained with our scheme are highly energetic and free from dispersive artifacts – a combination that has proven challenging to attain with the previously mentioned standard oceanographic approach. In summary, our approach achieves a noise-free higher “effective” resolution when compared to other state-of-the-art methods.

In sections 4 and 5, we tested our method in simple idealized solutions where we could precisely quantify the quality of the solutions. We wish to conclude here by illustrating that the W9V advection scheme shows promise when implemented in an “eddy-permitting” near-global ocean model. The simulation is performed on a latitude-longitude grid with a horizontal resolution of 1/12-th of a degree spanning from 75°S to 75°N, 100 vertical levels, and realistic topography. The model is initialized from rest with temperature and salinity fields obtained from the data-constrained ECCO state estimate version 4 (Forget et al., 2015). The heat and salt fluxes are computed by restoring to the ECCO surface temperature and salinity fields. The surface wind stress is also taken from ECCO. The simulation is run for ten years with a time step of 270 seconds. The W9V method results in a stable and noise-free solution at the same computational cost of the QGLEith method, and with the major advantage of requiring no tuning of parameters like a viscosity coefficient. Figure 1 shows the surface kinetic energy for the Gulf Stream and the Kuroshio current regions on March 1st, after 5 years of integration. The solution is characterized by a vigorous turbulence that comprises of a web of frontal currents, without any signature of grid-scale noise. This near-global solution is only intended to showcase the feasibility of the proposed advection scheme in a realistic “eddy-permitting” ocean simulation. A detailed analysis of the accuracy of the solution is left for future work.

Appendix A Explicit closures for SGS momentum fluxes

“Explicit” subgrid-scale closures are closures that rely on an explicit term to model the effect of unresolved scales on the filtered variables ($\nabla \cdot \tau_{SGS}$). Leveraging the downgradient principle, the additional term is usually expressed as a Laplacian diffusion of momentum,

$$\nabla \cdot \tau_{SGS} \approx \nabla \cdot (\nu_* \nabla u) , \quad (A1)$$

where ν_* is typically tuned to obtain the best fit to observations. While this approach ensures that principles (1)-(3) and (5) are satisfied, using a constant ν_* Laplacian diffusion leads to an excessively large dissipation and is contingent on the grid-size, failing to uphold principles (2) and (4). To enhance the selectivity of the SGS closure without compromising the simplicity of the implementation, Holland (1978) suggested the use of a biharmonic operator in place of the Laplacian, represented by:

$$\nabla \cdot \tau_{SGS} \approx -\nabla \cdot (\nu_* \nabla \nabla^2 u) . \quad (A2)$$

Despite the absence of a physical rationale for using a biharmonic operator instead of a Laplacian one, by better-upholding principles (2) and (4), this method has proven to be extremely successful in ocean simulations. In recent years, as computational power grew to allow increasingly higher-resolution simulations, there has been a surge in demand for new closures that can better adapt to varying resolutions. Most of the work has focused on finding a closed expression for a “scale-aware” effective viscosity ν_* (Griffies & Hallberg, 2000; Fox-Kemper & Menemenlis, 2004; Bachman et al., 2017) that can increase the selectivity by adapting to the different scales of the resolved flow. We briefly revisit two of the most successful “eddy” viscosity formulations: namely, the two-dimensional Leith closure and the quasi-geostrophic Leith closure, that we use as a point of comparison with our approach.

A1 Two-dimensional Leith closure

The Leith closure is specifically designed for two-dimensional turbulence, where enstrophy undergoes a forward cascade and is removed at small scales by viscous dissipation. The explicit form of the effective viscosity is derived from spectral scaling arguments, where the scaling of the Kolmogorov wavenumber in two-dimensional isotropic homogeneous turbulence follows (Kraichnan, 1967)

$$k \sim \eta^{1/6} \nu^{-1/2} . \quad (A3)$$

Here, η is the rate of cascade of enstrophy per unit area

$$\eta = \int_0^\infty \nu k^2 \mathcal{G} dk , \quad (\text{A4})$$

and $\mathcal{G}(k)$ is the enstrophy spectral density. The Leith closure (Leith, 1996) halts the enstrophy cascade at the maximum grid-resolved wavenumber (k_*) within the inertial range by assuming that the scaling in equation (A3) holds with the introduction of a suitable effective “eddy” viscosity (ν_*) for which

$$k_* \sim \eta_*^{1/6} \nu_*^{-1/2} \text{ and } \eta_* = \int_0^{k_*} \nu_* k^2 \mathcal{G} dk \approx \frac{1}{V} \int_V \nu_* |\nabla \zeta|^2 dV . \quad (\text{A5})$$

The last assumption of the Leith closure is the local homogeneity of flow properties, such that locally

$$\frac{1}{V} \int_V \nu_* |\nabla \zeta|^2 dV \sim \nu_* |\nabla \zeta|^2 . \quad (\text{A6})$$

Replacing k_* with $k_* \sim \pi/\Delta$ (where Δ is the grid spacing) leads to a closed form for the effective viscosity

$$\nu_* = \left(\frac{\mathbb{C}\Delta}{\pi} \right)^3 |\nabla \zeta| , \quad (\text{A7})$$

where \mathbb{C} is a tunable parameter of order 1.

A2 QG Leith closure

Building upon the principles of the original Leith subgrid-scale model, the quasi-geostrophic (QG) Leith model (Bachman et al., 2017; Pearson et al., 2017), expands its applicability specifically to the simulation of geophysical flows. Unlike the original Leith model, the QG Leith model accounts for the peculiar characteristics of geophysical turbulence, where potential vorticity, instead of two-dimensional vorticity, undergoes a forward cascade. To account for this difference, Bachman et al. (2017) propose to substitute the gradient of vertical vorticity in equation (A7) with the gradient of potential vorticity. Where quasi-geostrophic dynamics do not hold (e.g. on the equator or in mixed layers), the closure reverts to the classical two-dimensional Leith formulation. The effective viscosity in the QG Leith formulation is expressed by

$$\nu_* = \left(\frac{\mathbb{C}\Delta}{\pi} \right)^3 \left(\min(|\nabla q_1|, |\nabla q_2|, |\nabla q_3|)^2 + |\nabla(\nabla \cdot \mathbf{u})|^2 \right)^{1/2} , \quad (\text{A8})$$

where

$$\nabla q_1 = \nabla q + \partial_z \left(\frac{f}{N^2} \nabla b \right) , \quad \nabla q_2 = \nabla q \left(1 + \frac{1}{\text{Bu}} \right) , \quad \nabla q_3 = \nabla q \left(1 + \frac{1}{\text{Ro}^2} \right) , \quad (\text{A9})$$

and $\nabla q = \nabla(\zeta + f)$. Bu and Ro above are the grid-scale Burger and Rossby numbers,

$$\text{Bu} \stackrel{\text{def}}{=} \frac{\Delta^2}{L_d^2} \text{ and } \text{Ro} \stackrel{\text{def}}{=} \frac{V}{|f|\Delta} , \quad (\text{A10})$$

where V is a velocity scale (here assumed to be equal to 1)

Appendix B Discrete momentum advection on a staggered C-grid

As documented by Arakawa and Lamb (1977), the staggered C-grid is a widely utilized finite volume discretization method for atmospheric and ocean models. Its core principle involves averaging velocities and tracers onto separate grids, resulting in volumes that are staggered relative to one another. Figure B1 illustrates a two-dimensional (left) and three-dimensional (right) representation of the staggered C-grid, indicating the centers of the u , v ,

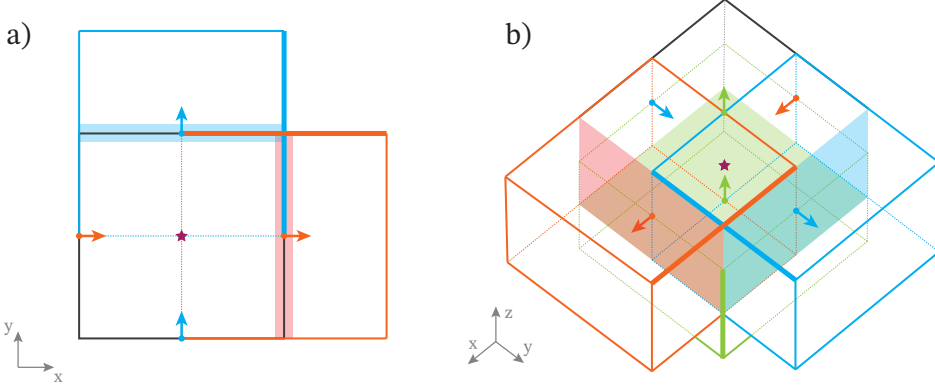


Figure B1. Depiction of the Arakawa staggered C-grid (Arakawa & Lamb, 1977). a) two-dimensional configuration, b) three-dimensional configuration. The red, blue, and green arrows represent u -, v - and w -velocity components, with the corresponding volumes \mathcal{V}_u , \mathcal{V}_v and \mathcal{V}_w delineated by red, blue and green lines, respectively. The shaded areas correspond to \mathcal{A}_x (red), \mathcal{A}_y (blue), and \mathcal{A}_z (green), while the thick lines indicate Δ_x (red), Δ_y (blue) and Δ_z (green). The purple star highlights the location of tracers and pressure, with the associated volume (\mathcal{V}_c) bounded by the shaded areas and the black lines.

and w velocity cells with arrows, while the star denotes the center of the tracer cell. In this work, we use the notation (connected to figure B1): The linear spacings and the facial areas of the u , v , and w velocity cells are denoted by Δ_x , Δ_y , Δ_z , and \mathcal{A}_x , \mathcal{A}_y , \mathcal{A}_z , respectively. The volumes of the u , v , and w velocity cells, as well as the tracer cells, are denoted by \mathcal{V}_u , \mathcal{V}_v , \mathcal{V}_w , and \mathcal{V}_c . We also use the δ , $\langle \cdot \rangle$, and $\{\cdot; \cdot\}$ notation to describe finite differences, centered reconstructions, and WENO reconstructions.

We express here the details of the implementations used in section 4 and 5. The discrete energy-conserving vorticity flux and centered vertical advection used in combination with the explicit closures described in the previous section read:

$$\mathcal{Z}_u^E = -\frac{\langle \langle \Delta_x v \rangle^i \zeta \rangle^j}{\Delta_x}, \quad \mathcal{Z}_v^E = \frac{\langle \langle \Delta_y u \rangle^j \zeta \rangle^i}{\Delta_y}, \quad (B1)$$

$$\mathcal{V}_u = \frac{\langle \langle W \rangle^j \delta_k u \rangle^k}{\mathcal{V}_u}, \quad \mathcal{V}_v = \frac{\langle \langle W \rangle^j \delta_k v \rangle^k}{\mathcal{V}_v} \quad (B2)$$

The discrete advection operators corresponding to the “ILES-inspired” WENO-based methodology described in this paper read:

$$\mathcal{Z}_u = -\frac{\langle \langle \Delta_x v \rangle \rangle^{ij}}{\Delta_x} \{\zeta; \mathbf{u}\}^j, \quad \mathcal{Z}_v = \frac{\langle \langle \Delta_y u \rangle \rangle^{ij}}{\Delta_y} \{\zeta; \mathbf{u}\}^i, \quad (B3)$$

$$\mathcal{C}_u = \frac{\delta_k \langle W \rangle^i \{u; u\}^k}{\mathcal{V}_u}, \quad \mathcal{C}_v = \frac{\delta_k \langle W \rangle^j \{v; v\}^k}{\mathcal{V}_v}, \quad (B4)$$

$$\mathcal{D}_u = \frac{u \{D; D\}^i}{\mathcal{V}_u}, \quad \mathcal{D}_v = \frac{v \{D; D\}^j}{\mathcal{V}_v}, \quad (B5)$$

$$\mathcal{K}_u = \frac{\left\{ \delta_i u^2; \langle u \rangle^i \right\}^i + \langle \delta_i v^2 \rangle^j}{\Delta_x}, \quad \mathcal{K}_v = \frac{\langle \delta_j u^2 \rangle^i + \left\{ \delta_j v^2; \langle v \rangle^j \right\}^j}{\Delta_y}. \quad (B6)$$

Appendix C Divergence flux, conservative vertical advection form

We set out to demonstrate that in terms of discrete kinetic energy conservation, \mathcal{V} is equivalent to $\mathcal{C} + \mathcal{D}$, or more specifically,

$$\sum_{i,j,k} (u\mathcal{V}_u\mathcal{V}_u + v\mathcal{V}_v\mathcal{V}_v) = \sum_{i,j,k} [u\mathcal{V}_u(\mathcal{C}_u + \mathcal{D}_u) + v\mathcal{V}_v(\mathcal{C}_v + \mathcal{D}_v)] . \quad (\text{C1})$$

Note that the influence of boundary fluxes is not taken into account in the following derivation. Given two fields ϕ and ψ defined on a staggered C-grid, centered second-order reconstructions and differences satisfy these pointwise properties (Adcroft et al., 1997)

$$\langle \psi \rangle^i \langle \phi \rangle^i = \langle \psi \phi \rangle^i - \frac{1}{4} \delta_i \psi \delta_i \phi , \quad (\text{C2})$$

$$\langle \delta_i \psi \rangle^i = \delta_i \langle \psi \rangle^i , \quad (\text{C3})$$

$$\langle \langle \psi \rangle^i \phi \rangle^i = \psi \langle \phi \rangle^i + \frac{1}{4} \delta_i (\phi \delta_i \psi) , \quad (\text{C4})$$

$$\delta_i (\langle \psi \rangle^i \phi) = \psi \delta_i \phi + \langle \phi \delta_i \psi \rangle^i , \quad (\text{C5})$$

and these integral properties (Madec et al., 2022)

$$\sum_i \psi \langle \phi \rangle^i = \sum_i \langle \psi \rangle^i \phi , \quad (\text{C6})$$

$$\sum_i \langle \psi \phi \rangle^i = \sum_i \psi \phi . \quad (\text{C7})$$

Note that the volumes associated with variables ϕ and ψ (denoting the “location” of the two quantities) are implied and not explicitly indicated. Combining (C6) with (C7) and (C2), we can derive an additional integral property

$$\sum_i \psi \langle \langle \phi \rangle^i \rangle^i = \sum_i \psi \phi - \frac{1}{4} \sum_i \delta_i \psi \delta_i \phi . \quad (\text{C8})$$

Focusing on the vertical advection term in the x-momentum equation (\mathcal{V}_u) and using property (C5):

$$\sum_{i,j,k} u\mathcal{V}_u \frac{\langle \langle W \rangle^i \delta_k u \rangle^k}{\mathcal{V}_u} = \underbrace{\sum_{i,j,k} u\mathcal{V}_u \frac{\langle \delta_k \langle \langle W \rangle^i \rangle^k u \rangle^k}{\mathcal{V}_u}}_{\text{term 1}} - \underbrace{\sum_{i,j,k} u\mathcal{V}_u \frac{\langle \langle u \delta_k \langle W \rangle^i \rangle^k \rangle^k}{\mathcal{V}_u}}_{\text{term 2}} . \quad (\text{C9})$$

Applying property (C3) followed by (C4) to term 1:

$$\text{term 1} = \sum_{i,j,k} u\mathcal{V}_u \underbrace{\frac{\delta_k \langle W \rangle^i \langle u \rangle^k}{\mathcal{V}_u}}_{\mathcal{C}_u} - \frac{1}{4} \sum_{i,j,k} u \delta_k \left(\delta_k \left(u \langle D \rangle^i \right) \right) . \quad (\text{C10})$$

where we made use of the discrete incompressibility condition ($D = -\delta_k W$). Applying the same incompressibility condition to term 2 followed by (C3) and (C8) yields

$$\text{term 2} = \sum_{i,j,k} u\mathcal{V}_u \underbrace{\frac{u \langle D \rangle^i}{\mathcal{V}_u}}_{\mathcal{D}_u} - \frac{1}{4} \sum_{i,j,k} (\delta_k u) \delta_k \left(u \langle D \rangle^i \right) . \quad (\text{C11})$$

Combining the two terms:

$$\sum_{i,j,k} u\mathcal{V}_u \mathcal{V}_u = \sum_{i,j,k} u\mathcal{V}_u (\mathcal{C}_u + \mathcal{D}_u) \quad (\text{C12})$$

$$- \frac{1}{4} \sum_{i,j,k} \left(u \delta_k \left(\delta_k \left(u \langle D \rangle^i \right) \right) + (\delta_k u) \delta_k \left(u \langle D \rangle^i \right) \right) . \quad (\text{C13})$$

Focusing on the second term on the RHS, using property (C7) on the second element in the summation yields

$$\sum_{i,j,k} u \mathcal{V}_u \mathcal{V}_u = \sum_{i,j,k} u \mathcal{V}_u (\mathcal{C}_u + \mathcal{D}_u) \quad (\text{C14})$$

$$- \frac{1}{4} \sum_{i,j,k} \left(u \delta_k (\delta_k (u \langle D \rangle^i)) + \langle (\delta_k u) \delta_k (u \langle D \rangle^i) \rangle^k \right). \quad (\text{C15})$$

The second term on the RHS can now be reduced using (C5), where $\psi = u$ and $\phi = \delta_k (u \langle D \rangle^i)$, leading to

$$\sum_{i,j,k} u \mathcal{V}_u \mathcal{V}_u = \sum_{i,j,k} u \mathcal{V}_u (\mathcal{C}_u + \mathcal{D}_u) - \frac{1}{4} \sum_{i,j,k} \delta_k \left(u \langle \delta_k (u \langle D \rangle^i) \rangle^k \right), \quad (\text{C16})$$

where the second term is the divergence of a vertical flux and, as such, its integral in the domain is equal to zero, leaving

$$\sum_{i,j,k} u \mathcal{V}_u \mathcal{V}_u = \sum_{i,j,k} u \mathcal{V}_u (\mathcal{C}_u + \mathcal{D}_u). \quad (\text{C17})$$

The same can be done for the v component leading to (C1).

Appendix D Upwinding of the discrete horizontal divergence

Contrary to vorticity reconstruction, straightforward upwinding of the horizontal divergence might not always lead to a decrease in discrete kinetic energy. To demonstrate this, we consider a first-order upwind reconstruction, for which

$$u \{c\}^i = u \langle c \rangle^i - \frac{|u|}{2} \delta_i c. \quad (\text{D1})$$

With the above reconstruction scheme, the discrete divergence flux is

$$u \frac{\{D\}^i}{\mathcal{V}_u} \hat{\mathbf{i}} + v \frac{\{D\}^j}{\mathcal{V}_v} \hat{\mathbf{j}} = \underbrace{\mathcal{D}_i \hat{\mathbf{i}} + \mathcal{D}_j \hat{\mathbf{j}}}_{\text{energy conserving}} - \underbrace{\left(|u| \frac{\delta_i D}{2 \mathcal{V}_u} \hat{\mathbf{i}} + |v| \frac{\delta_j D}{2 \mathcal{V}_v} \hat{\mathbf{j}} \right)}_{\text{not energy conserving}}. \quad (\text{D2})$$

The associated change in discrete integrated kinetic energy reads

$$\partial_t \sum_{i,j,k} (u^2 \mathcal{V}_u + v^2 \mathcal{V}_v + w^2 \mathcal{V}_w) = \quad (\text{D3})$$

$$= \underbrace{\sum_{i,j,k} (u|u|\delta_i \delta_i U + v|v|\delta_j \delta_j V)}_{\text{negative definite}} + \sum_{i,j,k} (u|u|\delta_i \delta_j V + v|v|\delta_j \delta_i U), \quad (\text{D4})$$

where D has been divided into its two components ($\delta_i U$ and $\delta_j V$). Using (C5), we can show that the first term on the RHS is negative definite:

$$u|u|\delta_i \delta_i U = \delta_i \left(\langle u|u| \rangle^i \delta_i U \right) - \langle u|\delta_i U \delta_i u \rangle^i - \langle u \delta_i U \delta_i |u| \rangle^i, \quad (\text{D5})$$

where the first term is the divergence of a flux and, provided that the discrete areas do not change drastically in neighboring cells,

$$u \delta_i U \delta_i |u| = |u| \delta_i U \delta_i u \geq 0. \quad (\text{D6})$$

The same can be shown for $v|v|\delta_j \delta_j V$. Assuming that horizontally divergent motions are small

$$\delta_i U \sim -\delta_j V, \quad (\text{D7})$$

the second term on the RHS of (D4) is

$$\sum_{i,j,k} (u|u|\delta_i\delta_j V + v|v|\delta_j\delta_i U) \sim - \sum_{i,j,k} (u|u|\delta_i\delta_i U + v|v|\delta_j\delta_j V) , \quad (\text{D8})$$

which is positive definite and counteracts the energy dissipation provided by the first term on the RHS of (D4). As such, upwinding the discrete divergence might have the undesired effect of injecting energy at the grid scale instead of removing it. To avoid adding kinetic energy at the grid scale, we apply a diffusive reconstruction only to the terms that lead to discrete energy dissipation (where the reconstruction direction is the same as the difference direction) while maintaining a centered reconstruction for the terms that could lead to energy production (where reconstruction and difference directions are perpendicular).

Open Research Section

The momentum advection scheme described in this paper is implemented in Oceananigans.jl (Ramadhan et al., 2020) starting from version 0.84.0. Visualizations were made using Makie.jl (Danisch & Krumbiegel, 2021). Scripts for reproducing the idealized baroclinic setups are available at github.com/simone-silvestri/BaroclinicAdjustment.jl.

Acknowledgments

Our work is supported by the generosity of Eric and Wendy Schmidt by recommendation of the Schmidt Futures program and by the National Science Foundation grant AGS-1835576. N.C.C. is supported by the Australian Research Council DECRA Fellowship DE210100749.

References

- Adcroft, A., Hill, C., & Marshall, J. (1997). Representation of topography by shaved cells in a height coordinate ocean model. *Monthly Weather Review*, 125(9), 2293-2315. doi: 10.1175/1520-0493(1997)125<2293:ROTBSC>2.0.CO;2
- Arakawa, A. (1966). Computational design for long-term numerical integration of the equations of fluid motion: Two-dimensional incompressible flow. Part I. *Journal of Computational Physics*, 1(1), 119-143. doi: 10.1016/0021-9991(66)90015-5
- Arakawa, A., & Lamb, V. (1977). Computational design of the basic dynamical processes of the UCLA general circulation model. In J. Chang (Ed.), *General circulation models of the atmosphere* (Vol. 17, p. 173-265). Elsevier. doi: 10.1016/B978-0-12-460817-7.50009-4
- Bachman, S., Fox-Kemper, B., & Pearson, B. (2017). A scale-aware subgrid model for quasi-geostrophic turbulence. *Journal of Geophysical Research: Oceans*. doi: 10.1002/2016JC012265
- Balsara, D., & Shu, C. (2000). Monotonicity preserving weighted essentially non-oscillatory schemes with increasingly high order of accuracy. *Journal of Computational Physics*, 160(2), 405-452. doi: 10.1006/jcph.2000.6443
- Bates, J. R., & McDonald, A. (1982). Multiply-upstream, semi-Lagrangian advective schemes: Analysis and application to a multi-level primitive equation model. *Monthly Weather Review*, 110(12), 1831-1842. doi: 10.1175/1520-0493(1982)110<1831:MUSLAS>2.0.CO;2
- Danisch, S., & Krumbiegel, J. (2021). Makie.jl: Flexible high-performance data visualization for Julia. *Journal of Open Source Software*, 6(65), 3349. doi: 10.21105/joss.03349
- Ding, M., Liu, H., Lin, P., Meng, Y., Zheng, W., An, B., ... Chen, K. (2022). A century-long eddy-resolving simulation of global oceanic large- and mesoscale state. *Scientific Data*, 9(1), 691. doi: 10.1038/s41597-022-01766-9
- Fenty, I., & Wang, O. (2020). *ECCO geometry parameters for the Lat-Lon-Cap 90 (llc90) native model grid (version 4 release 4)*. NASA Physical Oceanography Distributed

- Active Archive Center. Retrieved from https://podaac.jpl.nasa.gov/dataset/ECCO_L4_GEOMETRY_LLC0090GRID_V4R4 doi: 10.5067/ECL5A-GRD44
- Forget, G., Campin, J.-M., Heimbach, P., Hill, C., Ponte, R., & Wunsch, C. (2015). ECCO version 4: an integrated framework for non-linear inverse modeling and global ocean state estimation. *Geoscientific Model Development*, 8(10), 3071–3104. doi: 10.5194/gmd-8-3071-2015
- Fox-Kemper, B., & Menemenlis, D. (2004). Can large eddy simulation techniques improve mesoscale rich ocean models? In M. Hecht & H. Hasumi (Eds.), *Ocean modeling in an eddying regime* (pp. 319 – 337). doi: 10.1029/177GM19
- Gent, P., & Mcwilliams, J. (1990). Isopycnal mixing in ocean circulation models. *Journal of Physical Oceanography*, 20(1), 150-155. doi: 10.1175/1520-0485(1990)020<0150:IMIOCM>2.0.CO;2
- Griffies, S., & Hallberg, R. (2000). Biharmonic friction with a Smagorinsky-like viscosity for use in large-scale eddy-permitting ocean models. *Monthly Weather Review*, 128(8), 2935-2946. doi: 10.1175/1520-0493(2000)128<2935:BFWASL>2.0.CO;2
- Hahn, S., & Iaccarino, G. (2008). Simulations of vortex-dominated flows: adaptive vorticity confinement vs. rotational-form upwinding. *Center for Turbulence Research, Annual Research Brief*.
- Harten, A., Engquist, B., Osher, S., & Chakravarthy, S. (1987). Uniformly high order accurate essentially non-oscillatory schemes, III. *Journal of Computational Physics*, 71(2), 231-303. doi: 10.1016/0021-9991(87)90031-3
- Holland, W. (1978). The role of mesoscale eddies in the general circulation of the ocean—numerical experiments using a wind-driven quasi-geostrophic model. *Journal of Physical Oceanography*, 8(3), 363-392. doi: 10.1175/1520-0485(1978)008<0363:TROMEI>2.0.CO;2
- Holland, W., Chow, J., & Bryan, F. (1998). Application of a third-order upwind scheme in the NCAR ocean model. *Journal of Climate*, 11(6), 1487-1493. doi: 10.1175/1520-0442(1998)011<1487:AOATOU>2.0.CO;2
- Ishiko, K., Ohnishi, N., Ueno, K., & Sawada, K. (2009). Implicit large eddy simulation of two-dimensional homogeneous turbulence using weighted compact nonlinear scheme. *Journal of Fluids Engineering*. doi: 10.1115/1.3077141
- Juricke, S., Danilov, S., Kutsenko, A., & Oliver, M. (2019). Ocean kinetic energy backscatter parametrizations on unstructured grids: Impact on mesoscale turbulence in a channel. *Ocean Modelling*, 138, 51-67. doi: 10.1016/j.ocemod.2019.03.009
- Karaca, M., Lardjane, N., & Fedioun, I. (2012). Implicit large eddy simulation of high-speed non-reacting and reacting air/H₂ jets with a 5th order WENO scheme. *Computers & Fluids*, 62, 25-44. doi: 10.1016/j.compfluid.2012.03.013
- Kraichnan, R. (1967). Inertial ranges in two-dimensional turbulence. *The Physics of Fluids*, 10(7), 1417-1423. doi: 10.1063/1.1762301
- Leith, C. (1996). Stochastic models of chaotic systems. *Physica D: Nonlinear Phenomena*, 98(2), 481-491. (Nonlinear Phenomena in Ocean Dynamics) doi: 10.1016/0167-2789(96)00107-8
- Madec, G., Bourdallé-Badie, R., Chanut, J., Clementi, E., Coward, A., Ethé, C., ... Moulin, A. (2022, March). *NEMO ocean engine*. Zenodo. doi: 10.5281/zenodo.6334656
- Madec, G., & Imbard, M. (1996). A global ocean mesh to overcome the North pole singularity. *Climate Dynamics*, 12, 381-388. doi: 10.1007/BF00211684
- Maulik, R., & San, O. (2018). Explicit and implicit LES closures for Burgers turbulence. *Journal of Computational and Applied Mathematics*, 327, 12-40. doi: 10.1016/j.cam.2017.06.003
- Mohammadi-Aragh, M., Klingbeil, K., Brüggemann, N., Eden, C., & Burchard, H. (2015). The impact of advection schemes on lateral shear and baroclinic instabilities. *Ocean Modelling*, 94, 112–127. doi: 10.1016/j.ocemod.2015.07.021
- Norman, M. R., Eldred, C., & Meena, M. G. (2023). Investigating inherent numerical stabilization for the moist, compressible, non-hydrostatic euler equations on collocated grids. *Journal of Advances in Modeling Earth Systems*, 15(10), e2023MS003732. doi:

- 10.1029/2023MS003732
- Osher, S., & Shu, C. (1991). High-order essentially nonoscillatory schemes for Hamilton–Jacobi equations. *SIAM Journal on Numerical Analysis*, 28(4), 907-922. doi: 10.1137/0728049
- Pearson, B., Fox-Kemper, B., Bachman, S., & Bryan, F. (2017). Evaluation of scale-aware subgrid mesoscale eddy models in a global eddy-rich model. *Ocean Modelling*, 115, 42-58. doi: 10.1016/j.ocemod.2017.05.007
- Pressel, K., Mishra, S., Schneider, T., Kaul, M., & Tan, Z. (2017). Numerics and subgrid-scale modeling in large eddy simulations of stratocumulus clouds. *Journal of Advances in Modeling Earth Systems*, 9(2), 1342-1365. doi: 10.1002/2016MS000778
- Ramadhan, A., Wagner, G. L., Hill, C., Campin, J.-M., Churavy, V., Besard, T., ... Ferrari, R. (2020). Oceananigans.jl: Fast and friendly geophysical fluid dynamics on GPUs. *The Journal of Open Source Software*, 4(44), 1965. doi: 10.21105/joss.01965
- Ringler, T. D. (2011). Momentum, vorticity and transport: Considerations in the design of a finite-volume dynamical core. In P. Lauritzen, C. Jablonowski, M. Taylor, & R. Nair (Eds.), *Numerical techniques for global atmospheric models* (pp. 143–183). Berlin, Heidelberg: Springer Berlin Heidelberg. doi: 10.1007/978-3-642-11640-7_7
- Ronchi, C., Iacono, R., & Paolucci, P. (1996). The “cubed sphere”: A new method for the solution of partial differential equations in spherical geometry. *Journal of Computational Physics*, 124(1), 93-114. doi: 10.1006/jcph.1996.0047
- Roulet, G., & Gaillard, T. (2022). A fast monotone discretization of the rotating shallow water equations. *Journal of Advances in Modeling Earth Systems*. doi: 10.1029/2021MS002663
- Shchepetkin, A., & McWilliams, J. (1998a). Quasi-monotone advection schemes based on explicit locally adaptive dissipation. *Monthly Weather Review*, 126(6), 1541-1580. doi: 10.1175/1520-0493(1998)126<1541:QMASBO>2.0.CO;2
- Shchepetkin, A., & McWilliams, J. C. (1998b). Quasi-monotone advection schemes based on explicit locally adaptive dissipation. *Monthly Weather Rev*, 126, 1541-1580.
- Shu, C. (1997). *Essentially non-oscillatory and weighted essentially non-oscillatory schemes for hyperbolic conservation laws* (ICASE Report No. 97-65). Institute for Computer Applications in Science and Engineering, NASA Langley Research Center.
- Silvestri, S., Wagner, G. L., Hill, C. N., Ardakani, M. R., Blaschke, J., Campin, J.-M., ... Ferrari, R. (2023). Oceananigans.jl: A model that achieves breakthrough resolution, memory and energy efficiency in global ocean simulations. (arXiv:2309.06662) doi: 10.48550/arXiv.2309.06662
- Smagorinsky, J. (1963). General circulation experiments with the primitive equations: I. the basic experiment. *Monthly Weather Review*, 91(3), 99-164. doi: 10.1175/1520-0493(1963)091<0099:GCEWTP>2.3.CO;2
- Smolarkiewicz, P., & Margolin, L. (1998). MPDATA: A finite-difference solver for geophysical flows. *Journal of Computational Physics*, 140(2), 459-480. doi: 10.1006/jcph.1998.5901
- Soufflet, Y., Marchesiello, P., Lemarié, F., Jouanno, J., Capet, X., Debreu, L., & Benshila, R. (2016). On effective resolution in ocean models. *Ocean Modelling*, 98, 36-50. doi: 10.1016/j.ocemod.2015.12.004
- Souza, A., He, J., Bischoff, T., Waruszewski, M., Novak, L., Barra, V., ... Schneider, T. (2023). The flux-differencing discontinuous galerkin method applied to an idealized fully compressible nonhydrostatic dry atmosphere. *Journal of Advances in Modeling Earth Systems*, 15(4), e2022MS003527. doi: 10.1029/2022MS003527
- Sytine, I., Porter, D., Woodward, P., Hodson, S., & Winkler, K.-H. (2000). Convergence tests for the piecewise parabolic method and Navier–Stokes solutions for homogeneous compressible turbulence. *Journal of Computational Physics*, 158(2), 225-238. doi: 10.1006/jcph.1999.6416
- Vallis, G. K. (2017). *Atmospheric and oceanic fluid dynamics*. Cambridge University Press.
- Van Leer, B. (1977). Towards the ultimate conservative difference scheme. IV. A new approach to numerical convection. *Journal of Computational Physics*, 23(3), 276-299. doi: 10.1016/0021-9991(77)90095-X

- Woodward, P., & Colella, P. (1984). The numerical simulation of two-dimensional fluid flow with strong shocks. *Journal of Computational Physics*, 54(1), 115-173. doi: 10.1016/0021-9991(84)90142-6
- Zalesak, S. (1979). Fully multidimensional flux-corrected transport algorithms for fluids. *Journal of Computational Physics*, 31(3), 335-362. doi: 10.1016/0021-9991(79)90051-2
- Zeng, K., Li, Z., Rana, Z., & Jenkins, K. (2021). Implicit large eddy simulations of turbulent flow around a square cylinder at $\text{Re}=22,000$. *Computers & Fluids*, 226, 105000. doi: 10.1016/j.compfluid.2021.105000